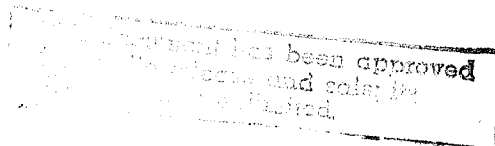


APPLICATIONS OF SPECTRAL MICROWAVE RADIOMETRY TO
SENSING OF SEA ICE AND THE OCEAN SURFACE

A Dissertation Presented

by

KAREN M. ST. GERMAIN



Submitted to the Graduate School of the
University of Massachusetts in partial fulfillment
of the requirements for the degree of

DOCTOR OF PHILOSOPHY

May 1993

Department of Electrical and Computer Engineering

19941223 064

List For	
CH&I	<input checked="" type="checkbox"/>
...	<input type="checkbox"/>
...	<input type="checkbox"/>

A-1

© Copyright Karen M. St.Germain 1993

All Rights Reserved

APPLICATIONS OF SPECTRAL MICROWAVE RADIOMETRY TO
SENSING OF SEA ICE AND THE OCEAN SURFACE

A Dissertation Presented

by

KAREN M. ST.GERMAIN

Approved as to style and content by:

Calvin T. Swift, Chair

Robert E. McIntosh, Member

Daniel H. Schaubert, Member

Julie Brigham-Grette, Member, Geology & Geography

Keith R. Carver, Department Head
Electrical & Computer Engineering

This dissertation is dedicated to my parents, Richard and Alice,
who have never reminded me that I said I could do it by myself.

ACKNOWLEDGEMENTS

I wish to thank Dr. Calvin Swift and Dr. Robert McIntosh for giving me the opportunity to join their efforts in the Microwave Remote Sensing Laboratory. In particular, I am grateful to Dr. Swift for his trust, encouragement, and the many hours he invested. I would also like to thank Dr. Mark Goodberlet for his patience, insight, and consistent willingness to help, and Dr. Ivan Popstefanija for generously sharing his computer and hardware expertise. The time and helpful suggestions provided by my committee members, Drs. Julie Brigham-Grette and Daniel Shaubert are also very much appreciated.

I would like to acknowledge Dr. Ron Lindsay for providing the AVHRR derived ice temperatures, and the National Snow and Ice Data Center for providing the SSM/I data. Thanks are also due to a number of outside members of the remote sensing community, including Dr. Tom Grenfell and Dr. Dale Winebrenner of the University of Washington for offering their expertise and insights.

Special thanks to Dave Parker and Linda Klemyk for computer and logistics support, which went above and beyond the call of duty on more than one occasion. I would also like to acknowledge the other members of MIRSL, particularly Peter Gaiser, Jonas Aleksa, Paul Chang, and Karen Heatherington, who contributed to my work (and good humor) in a variety of ways.

ABSTRACT

APPLICATIONS OF SPECTRAL MICROWAVE RADIOMETRY TO SENSING OF SEA ICE AND THE OCEAN SURFACE

MAY 1993

KAREN M. ST.GERMAIN

B.S.E.E., UNION COLLEGE

PH.D., UNIVERSITY OF MASSACHUSETTS, AMHERST, MASSACHUSETTS

Directed by: Professor Calvin T. Swift

The dielectric properties and emissivity of several types of sea ice were studied to improve upon the currently available algorithms for interpreting polar radiometric imagery from the SSM/I sensor. Laboratory studies indicated that the relative dielectric constant of new sea ice, as measured with a spectral C-Band radiometer, is approximately 12. This value represents the early stages of ice formation, and decreases rapidly with ice growth to approach the accepted value of 3.2 for first year ice. Atmospheric effects on satellite based passive microwave data were also examined with regard to the 19, 22, 37, and 85 GHz channels of the SSM/I system. The atmospheric vapor and cloud liquid water attenuation was empirically modeled with respect to frequency and atmospheric temperature. The mean atmospheric temperature was empirically linked to surface temperature through an exponential relationship. The surface emissivity was then modelled as a function of surface type via a mixing formalism, where the emissivity of open water depends on surface wind-speed. With the significant environmental variables parameterized, two algorithms for analysis of polar SSM/I data were developed. The first is a simple modification that adds the capability of determining ice temperature to an existing algorithm. The second is a weather correcting algorithm significantly more complex than those currently in use for the lower three frequencies of the Special Sensor Microwave

Imager (SSM/I). The uncertainty of the six products due to measurement noise was estimated at 5% for surface parameters and 10% for atmospheric variables. The atmospheric vapor and cloud liquid water estimates are used to convert the raw 85 GHz brightness temperatures to surface brightness temperature estimates, producing a significantly enhanced ice edge.

TABLE OF CONTENTS

	<u>Page</u>
ACKNOWLEDGEMENTS	v
LIST OF TABLES	x
LIST OF FIGURES	xi
CHAPTERS	
1. INTRODUCTION	1
1.1 The Polar Regions and Remote Sensing	2
2. DIELECTRIC PROPERTIES AND EMISSIVITY OF SEA ICE	5
2.1 Review of Radiative Transfer Theory	5
2.2 New Ice	6
2.2.1 Radiometric Emission from Layered Media	7
2.2.2 Experiment Description and Data	10
2.2.3 Determination of the Dielectric Constant	10
2.2.4 Summary of New Ice Characteristics	19
2.3 First Year Ice	19
2.4 Multiyear Ice	22
3. EMISSION FROM THE ATMOSPHERE	26
3.1 Application of Radiative Transfer Theory To The Atmosphere . . .	26
3.1.1 Microwave Brightness Temperature Equation in a tropical hurricane case study	30
3.1.2 Microwave Brightness Temperature Equation in a polar case study	34
4. SSM/I ALGORITHMS	39
4.1 Review of Previous and Current Algorithms	39
4.1.1 Ice Type and Concentration	39
4.1.2 Ice Temperature	41
4.2 Modification to the NASA Team Algorithm	43
4.2.1 Algorithm Description	43
4.2.2 Temperature Evaluation	45

4.3	Weather Correcting Decision Algorithm	56
4.3.1	Algorithm Description	56
4.3.2	Algorithm Product Evaluation	60
4.3.3	Sensitivity Analysis	71
4.3.4	Implications for an 85 GHz high resolution mode	74
5.	CONCLUSION	83
	APPENDIX: SFMR WINDSPEED ALGORITHM	86
	REFERENCES	91

LIST OF TABLES

Table		Page
2.1	Mean ice thicknesses measured at the first maximum $d/\lambda = 0.25$ and first minimum $d/\lambda = 0.50$ in the time series brightness temperature data for each frequency.	14
4.1	Emissivity tie points used in the modification to the SSM/I team algorithm.	44
4.2	Coefficients relating 20m windspeed to surface roughness, σ	58
4.3	Coefficients relating 20m windspeed to foam fraction, FF	58
4.4	Coefficients relating roughness, σ , and foam fraction, FF , to open water emissivity.	59
4.5	Typical standard deviation of instrument noise for each SSM/I channel in Kelvins.	73
4.6	Standard deviation of algorithm products as a result of noise introduced on the brightness temperature data.	73
4.7	Standard deviation of algorithm products as a result emissivity errors.	73
A.1	Atmospheric opacity for each of the SFMR frequencies	89

LIST OF FIGURES

Figure	Page
2.1 Geometry of emission from a layered structure such as ice over water.	8
2.2 Emissivity of sheet 1B as a function of ice thickness at vertical polarization for 18, 37 and 90 GHz.	11
2.3 Brightness temperature of sheet 1B as a function of ice thickness at horizontal polarization at the six C-band frequencies of the Stepped Frequency Microwave Radiometer.	12
2.4 Calculated dielectric constant as a function of ice thickness. .	16
2.5 Salinity profile of sheet 1A for each day from January 5 through January 7, 1988.	17
2.6 Dielectric constant as a function of frequency for first-year ice and multiyear ice. Computed based on typical values of density and dielectric constant [1].	20
2.7 Typical geometry for first-year ice [2].	21
2.8 Typical geometry for multiyear ice [2].	23
2.9 Comparison of measured nadir emissivity of multiyear ice with theoretical calculations [2].	25
3.1 Schematic representation of the radiative transfer equation [1].	29
4.1 Temperature derived from the modified Team algorithm versus buoy temperatures supplied by the Arctic Ocean Buoy Program. The data set includes data from all operational buoys for every odd day in March, 1988	46
4.2 AVHRR Arctic Grids. Identified as 'Pacific' and 'European', the grids have 1 Km ² resolution [3].	48
4.3 Ice/snow surface temperature derived from the AVHRR thermal channels. Black area is masked for clouds.	49

4.4	AVHRR temperatures degraded to the 25 Km ² resolution of the SSM/I polar grid.	50
4.5	SSM/I derived temperatures corresponding to the AVHRR image in Figure 4.3	51
4.6	Cluster plot corresponding to the temperatures presented in Figures 4.4 and 4.5.	52
4.7	Cluster plot including all of the thirteen 512Km ² study areas.	53
4.8	Difference between SSM/I derived temperatures and AVHRR derived temperatures plotted versus retrieved water concentration for the thirteen 512Km ² study areas.	55
4.9	Schematic representation of the Decision routine that decides which of the six possible variables, (C_{FY} , C_{MY} , W , T_S , V , L), should be of primary concern for a given pixel.	61
4.10	Integrated Atmospheric Water Vapor derived from the Decision Algorithm for March 11, 1988	63
4.11	Visible frequency image from AVHRR. The region of interest is the white rectangular cloud in the Beaufort Sea.	64
4.12	Infrared image from AVHRR. The area of interest appears as a dark (warm) rectangle in the Beaufort Sea.	65
4.13	Image of ice temperature retrieval for March 11, 1988. Land has been masked in black.	66
4.14	Average temperature contours for March [4].	67
4.15	Scatter plot of ice temperature as retrieved by the Decision Algorithm vs. air temperature measured by AOBP Buoys in March, 1988. The slope of the regression line is 0.78, the correlation coefficient is 0.78 and the rms difference is 4.9K	68
4.16	Time series comparison for every odd day in March, 1988	69
4.17	Difference between SSM/I derived temperature and AVHRR derived temperature plotted versus retrieved water concentration (0 - 50%)	70
4.18	Arctic brightness temperatures at 85 GHz horizontal polarization.	76

4.19	Arctic brightness temperatures at 85 GHz horizontal polarization corrected for atmospheric vapor and cloud liquid water.	78
4.20	Total ice concentration as derived from the decision algorithm for the Greenland Sea on April 25, 1988	79
4.21	Brightness Temperature at 85 GHz horizontal polarization in the Greenland Sea on April 25, 1988	80
4.22	Surface brightness temperature at 85 GHz horizontal polarization. The atmospheric attenuation was calculated from the integrated cloud liquid water and atmospheric vapor estimates from the decision algorithm.	81
A.1	Flow diagram for the windspeed algorithm used to calculate ocean surface windspeed and rain rate from SFMR data . . .	90

CHAPTER 1

INTRODUCTION

At a time when global climate change and environmental issues are dominating many of the science disciplines, the synoptic and often global capabilities of remote sensing are contributing in new ways to many of the more traditional sciences. Active remote sensing, in the form of microwave weather radar, and passive remote sensing with infra-red and visible frequency systems are familiar examples of the role of remote sensing in meteorology and climatology. Microwave radiometry is less familiar to many, even though its development dates back to the 1930s. Because radars rely on electromagnetic reflection and radiometers rely on emission, passive and active remote sensing are inherently complementary.

In the 1930s and 1940s the field of microwave radiometry was developed by the radioastronomy community as a means of measuring electromagnetic energy originating from outside our solar system. It wasn't, however, until the late 1950s that such instruments were used in terrestrial observations [1]. Over the last several decades the development of satellite based sensors has enabled the remote sensing community to investigate global as well as local phenomena.

This dissertation addresses several environmental applications of microwave radiometry. Although the geophysical variables are very different, the measurement and analysis techniques are remarkably similar. In each case, a multi-frequency, or spectral, approach is taken to account for as many changing parameters as possible. Careful correction for atmospheric effects is crucial to all radiometric measurements and is a recurring theme throughout this work.

1.1 The Polar Regions and Remote Sensing

Polar sea ice covers approximately 7% of the world's oceans. In the Antarctic the sea ice spatial extent varies between $4.0 \times 10^6 \text{ km}^2$ during summer and $20.0 \times 10^6 \text{ km}^2$ during winter, while in the Arctic the variation is significantly less, from 7.8×10^6 to $14.8 \times 10^6 \text{ km}^2$. This coverage has a tremendous impact on the global climate. During the summer sea ice reflects roughly five times more solar radiation than does sea water, and the melting process absorbs energy from the atmosphere. The effect of these processes is to cool the hemisphere during its warmest months. Conversely, during the winter the heat flux from water to atmosphere is approximately two orders of magnitude greater than the heat flux through ice. Thus, the sea ice acts as an insulator during the winter. In addition, the freezing process releases energy into the atmosphere, effectively damping seasonal temperature swings [5].

The ice edge is also an important region of biological activity. It is at the ice edge that krill production takes place, which is crucial as the foundation for the food chain in the world's oceans. Practically, the sea ice affects commercial shipping routes and the construction of oil extraction platforms. Sea ice also modifies submarine acoustics, making knowledge of extent, thickness, and roughness crucial to underwater navigation. The latter two parameters are strongly related to ice type.

There are many types of sea ice, from the thin ice types (grease ice, nilas, pancake ice, etc.) to thick multi-year ice. Each ice type has a unique microwave signature which is a function primarily of dielectric constant. The dielectric constant of ice is dependent on several parameters, most notably salinity and temperature [2]. Because salinity decreases with ice age, especially after a summer surface melt, it is possible to classify ice in terms of two broad categories, first-year ice and multiyear ice, which are distinguishable from a satellite [5].

Interpretation of data from satellite based instruments has been aided over the years by many ground based experiments. CEAREX, LIMEX, and LEADEx occurred in 'the field', while others occurred in a more controlled laboratory environment. One example of the latter is the CRRELEX series which takes place annually at the United States Army Cold Regions Research and Engineering Laboratory in Hanover, New Hampshire. The CRRELEX program was initiated by the Office of Naval Research to study the dielectric properties of sea ice as they relate to growth conditions, thermal cycling, and precipitation [6], [7]. Chapter 2 analyzes the data from one such experiment. The growth phase of a sheet of saline ice was observed with a multifrequency radiometer at several angles of incidence [8]. The resulting measurements yielded new estimates of the dielectric properties of the surface during the transition from water to saline ice [9]. Chapter 2 also reviews the electromagnetic properties of first-year ice and multiyear ice, which are used in the following chapters.

In 1972 the Electrically Scanned Microwave Radiometer (ESMR) was sent into orbit aboard the Nimbus 5 satellite. This instrument produced the first global measurements of sea-ice extent, concentration, and type in the polar regions, as well as rain rate estimates in the lower latitudes. ESMR was followed in 1978 by the Scanning Multi-channel Microwave Radiometer (SMMR) aboard the Nimbus 7 and Seasat satellites. The multi-frequency design of SMMR offered several advantages over the single channel ESMR, in particular increased ability to reduce ambiguities introduced by ice type and atmospheric phenomena [10]. The SMMR instrument suffered from gain drift and thermal problems however, which seriously limited its utility.

The Special Sensor Microwave Imager (SSM/I) was launched in 1987 as part of the Defense Meteorological Satellite Program [11]. An extensive calibration and validation effort insured that the SSM/I would be the most accurate multi-channel

radiometer orbiting to date [12]. The instrument is linearly polarized at four frequencies: 19 GHz, 22 GHz, 37 GHz, and 85 GHz. The SSM/I data responds to global ocean surface winds and sea-ice conditions, as well as atmospheric effects which must be modeled [13]. A review of radiative transfer theory applied to the atmosphere is presented in Chapter 3, and the atmospheric attenuation is modeled as a function of integrated atmospheric vapor and integrated cloud liquid water.

Building on Chapters 2 and 3, Chapter 4 is dedicated to the development of algorithms for interpreting SSM/I data to extract sea ice concentration, type, and temperature in the Arctic. After a brief review of previous and currently available algorithms [14], the chapter describes two new algorithms developed for analyzing polar SSM/I data at the lower three frequencies. The first is a simple modification that adds the capability of determining ice temperature to an existing algorithm. The second is a weather-correcting algorithm significantly more complex than those currently in use. This algorithm corrects for atmospheric effects; its goal is to assist in the interpretation of higher resolution 85 GHz data. Both algorithms are shown to significantly increase the amount of geophysical information that can be extracted from the SSM/I brightness temperatures.

CHAPTER 2

DIELECTRIC PROPERTIES AND EMISSIVITY OF SEA ICE

2.1 Review of Radiative Transfer Theory

Radiation transfer within a half-space has been described and applied to passive remote sensing measurements for the past 15 years. When multiple scattering is ignored, the radiation transfer equation simplifies from an integrodifferential equation to an ordinary differential equation. The solution for the upwelling brightness temperature at height h is:

$$T_B(h) = \int_0^h T(z) \alpha_a(z) e^{-\int_0^z [\alpha_a(z') + \alpha_s(z')] dz'} dz \quad (2.1)$$

where $T(z)$ is the physical temperature at height h , α_a is the attenuation coefficient, and α_s is the scattering coefficient. An approximate solution of Equation 2.1 may be obtained by assuming constant temperature, attenuation and scattering with h :

$$T_B(h) = T_{PHYS} \alpha_a \int_0^h e^{-z(\alpha_a + \alpha_s)} dz \quad (2.2)$$

$$\approx T_{PHYS} \left(\frac{\alpha_a}{\alpha_s + \alpha_a} \right) \quad (2.3)$$

At the half-space boundary some of the radiation is reflected and, when the surface is in thermal equilibrium, the remainder is emitted:

$$T_B = \frac{(1 - r) T_{PHYS}}{1 + \alpha_s / \alpha_a} \quad (2.4)$$

where r is the Fresnel reflection coefficient due to the mismatch. When the scattering coefficient is zero, this relationship reduces to:

$$T_B = e T_{PHYS} \quad (2.5)$$

for emissivity, e . This is a reasonable approximation for homogeneous materials such as new ice and first-year ice, which are presented in Sections 2.2 and 2.3.

Multiyear ice, however, contains air bubbles with diameters approximately equal to wavelength at microwave frequencies. These bubbles are of sufficient density to increase the scattering coefficient significantly, and Equation 2.4 must be used instead of 2.5. This case is discussed in greater detail in Section 2.4

2.2 New Ice

As sea water freezes, brine pockets form between the growing ice crystals. As crystal growth continues, some of the brine may be expelled to the ice surface and to the sea water below, while some remains trapped between crystals. During this early stage the surface and trapped brine dominate the dielectric properties of the ice, but the dielectric constant is difficult to measure directly because, at thicknesses of only a centimeter or so, the ice is structurally weak. To address this issue, in 1980 a facility, which has been described several times in open literature [7],[6],[15], was constructed at the U.S. Army Cold Regions Research and Engineering Laboratory (CRREL).

An experiment conducted at CRREL provided the first remotely determined measurements of the dielectric constant of sub-centimeter saline ice. Emission was measured across C-Band (4-8 GHz) during the growth of a saline ice sheet. The data were collected with the Stepped Frequency Microwave Radiometer (SFMR) as part of a cooperative experiment. Data at the six frequencies of the SFMR exhibited oscillatory behavior as the ice sheet developed, which indicates a coherent effect in the emission. Ice thickness and angle of incidence were monitored continuously, making it possible to infer the dielectric constant of the sheet at ice thicknesses corresponding to local brightness temperature maxima and minima. To understand the method, a brief review of emission from layered media is necessary.

2.2.1 Radiometric Emission from Layered Media

Although thermal emission is a random process, constructive and destructive interference occurs as a result of the path length difference between reflection of the wave occurring at the two boundaries. Radiometric emission from layered media has been approached from two viewpoints [1]. The coherent approach is based upon solutions to Maxwell's equations, and accounts for both the magnitudes and phases of the electromagnetic fields reflected within the layered structure shown in Figure 2.1. Alternatively, the incoherent approach is based upon radiative transfer theory, which does not preserve phase, and results in a simpler expression that approximates the radiometric emission when irregular boundaries, finite receiver bandwidth, or the antenna beamwidth reduce coherence.

For a layer characterized by dielectric constant ϵ_1 , and thickness d_o over a half space of different dielectric constant ϵ_2 , the emissivity e , as derived from the Fresnel boundary-value problem (coherent approach), is given by:

$$e = 1 - r = \frac{(1 - r_i)(1 - Ar_w)}{1 + Ar_i r_w + 2\sqrt{Ar_i r_w} \cos(2\beta d_o)} \quad (2.6)$$

where,

- r = reflectivity of the composite structure
- r_i = reflection coefficient of air to medium 1
- r_w = reflection coefficient of medium 1 to medium 2
- β = $\frac{2\pi}{\lambda}$ phase constant where λ is the wavelength in medium 1
- A = $\exp(-4\alpha d_o)$ where α is the attenuation coefficient in medium 1

A form of this equation is given in Chapter 4 of Ulaby, Moore and Fung [1], and, for simplicity, assumes real voltage reflection coefficients and a low loss tangent to reduce the complexity of the phase term.

Equation 2.6 shows that the emissivity is a periodic function of slab thickness when the loss is negligible. Maxima occur when $\cos 2\beta d_o = -1$ and minima occur when $\cos 2\beta d_o = +1$. These values respectively correspond to odd and even quarter-wavelength intervals of layer thickness. When the slab is lossy (large α), periodicity

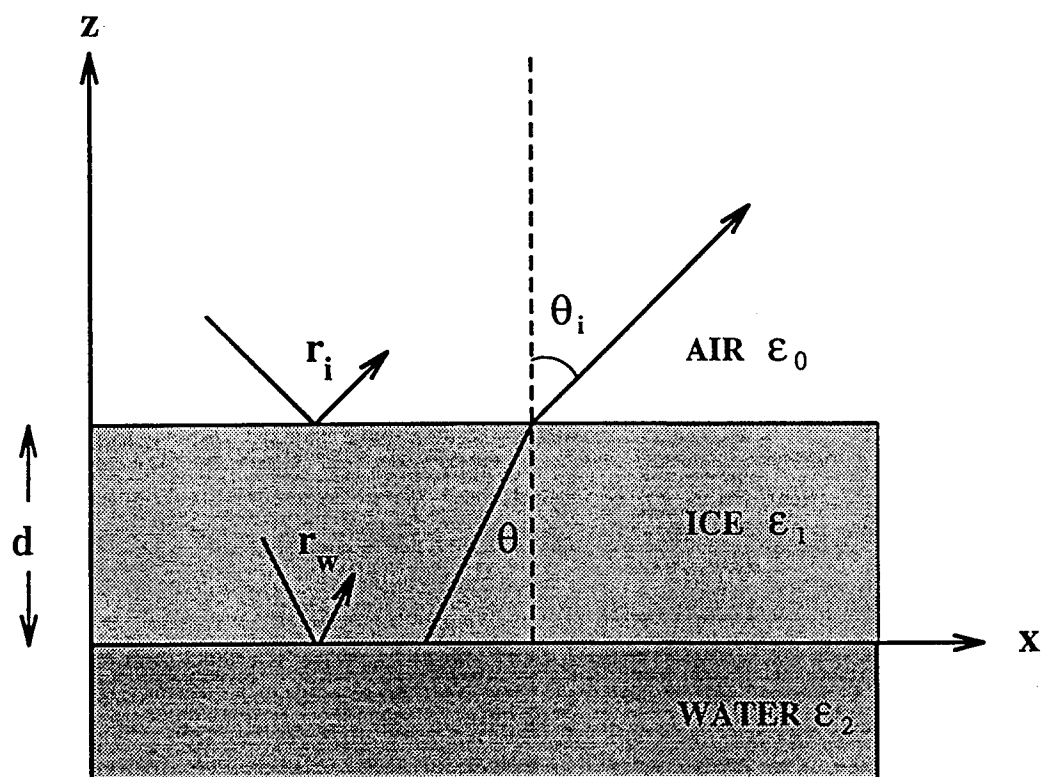


Figure 2.1. Geometry of emission from a layered structure such as ice over water.

still occurs; however, the excursions between maxima and minima are damped out by the attenuation term in Equation 2.6.

If the slab is viewed at an angle of incidence, the quarter-wave oscillation will still occur; however, the equivalent path length within the ice is increased by $\cos \theta_t$, where θ_t is the angle of transmission into the slab. The optical path length d through the ice, in terms of the wavelength is given by:

$$\frac{d}{\lambda_i} = \frac{f d_o \sqrt{\epsilon'_i}}{c \cos \theta_t} \quad (2.7)$$

where ϵ'_i is the dielectric constant of the ice, d_o is the mean thickness, c is the speed of light, and f is the frequency. The angle of refraction is described by Snell's law as:

$$\cos \theta_t = \sqrt{1 - \frac{\sin^2 \theta_i}{\epsilon'_i}} \quad (2.8)$$

These two equations can be combined to yield:

$$\frac{d}{\lambda_i} = \frac{f d_o \sqrt{\epsilon'_i}}{c \sqrt{1 - \frac{\sin^2 \theta_i}{\epsilon'_i}}} \quad (2.9)$$

Using the quadratic formula, it is now possible to solve for the dielectric constant in terms of known quantities:

$$\epsilon'_i = \frac{1}{2} \left\{ \left(\frac{cd}{d_o f \lambda_i} \right)^2 \pm \sqrt{\left(\frac{cd}{d_o f \lambda_i} \right)^4 - 4 \left(\frac{cd}{d_o f \lambda_i} \right)^2 \sin^2 \theta_i} \right\} \quad (2.10)$$

For a given frequency and angle of incidence, ϵ'_i , λ_i , d , and d_o are the only unknowns in Equation 2.10. At the first local maximum, $\frac{d}{\lambda_i} = 0.25$ and at the first local minimum, $\frac{d}{\lambda_i} = 0.50$. Multiple frequencies may be employed to solve for the remaining two variables. If d_o is measured continuously, ϵ'_i is the only unknown and may be calculated explicitly. The root corresponding to the negative sign can be ruled out because it yields values of relative dielectric constant that are less than one, and thus not physically reasonable.

2.2.2 Experiment Description and Data

Three ice sheets were grown in the CRREL facility during a period of cold weather that extended from December 29, 1987 to January 8, 1988 (CRRELEX 88). The ice thickness was monitored by periodically extracting ice samples. The sheet dedicated to passive microwave radiometry (designated as sheet 1B) grew from 0 to 6 cm over 22 hours on January 7 and 8, 1988. The air temperature was approximately -20° C and the atmosphere was clear and calm. These conditions gave rise to a visibly smooth and uniformly thick sheet of congelation ice. Single frequency radiometers operating at 10, 18.7, 37 and 90 GHz collected data throughout the growth phase. To cover C-band and investigate the possibility of coherent emission, the SFMR was also used. The SFMR is a spectral radiometer that can be tuned to operate at any frequency within the 4 to 8 GHz band. For this experiment, six frequencies were monitored: 4.63, 5.05, 5.91, 6.33, 6.76, and 7.20 GHz. The bandwidth at each frequency was 100 MHz, and the time required to scan all frequencies was approximately 1 minute. Data were collected continuously for the first several hours of growth, and then at 15 minute intervals as the ice thickness increased. The SFMR was pointed at an angle of 35 degrees off nadir, while the single frequency radiometers scanned in angle from 30 to 50 degrees off nadir. Variation of the ice emissivity with thickness during the growth phase is shown in Figure 2.2 for frequencies of 18.7, 37, and 90 GHz. A plot of the concurrent SFMR data is presented in Figure 2.3.

2.2.3 Determination of the Dielectric Constant

The signatures measured by the single-frequency radiometers are characterized by a rapid increase in emissivity with increasing ice thickness up to a saturation

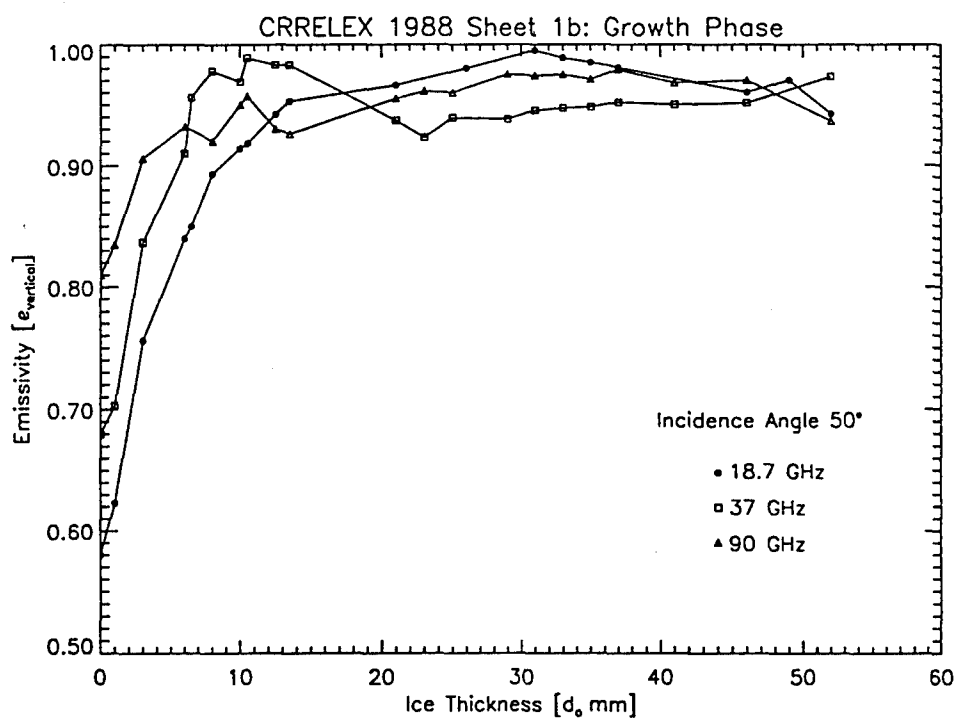


Figure 2.2. Emissivity of sheet 1B as a function of ice thickness at vertical polarization for 18, 37 and 90 GHz.

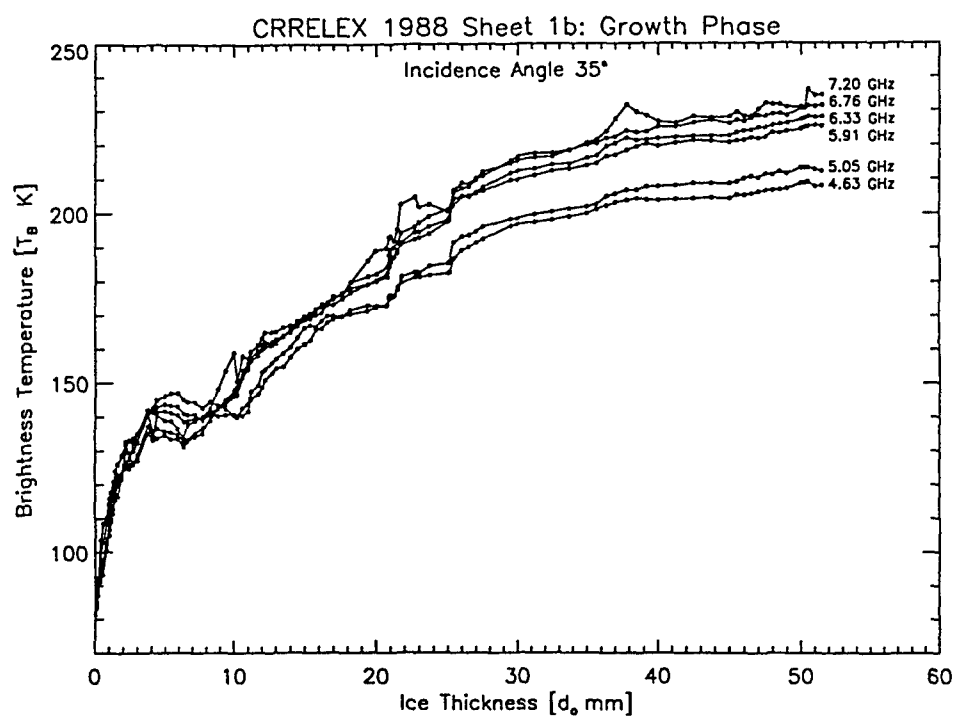


Figure 2.3. Brightness temperature of sheet 1B as a function of ice thickness at horizontal polarization at the six C-band frequencies of the Stepped Frequency Microwave Radiometer.

point. The extinction coefficient of the ice depends strongly on the observational frequency and determines the ice penetration depth. To show this effect more clearly and assuming negligible volume scattering, the attenuation coefficient of the ice, A , from Equation 2.6, can be re-expressed as:

$$A = \exp(-4\alpha d) = \exp\left(\frac{-8\pi n_i d}{\lambda_o}\right) \quad (2.11)$$

where n_i is the imaginary part of the index of refraction of sea ice. Because n_i is expected to be nearly constant over the microwave band of frequencies, Equation 2.11 shows that the ice attenuation increases as the free-space wavelength decreases, indicating that for a given ice thickness (constant d), the emission from the underlying water diminishes as the operating frequency is increased (λ_o decreased). This is consistent with the data trends in Figure 2.2, where brightness temperature increases with frequency.

As with the higher frequencies, the SFMR brightness temperatures increase with ice thickness, but the C-band wavelength is so much larger that saturation does not occur until the ice is substantially thicker. This agrees with previously published results [[6],[8]] which discuss noncoherent behavior. Notice, however, the brightness temperature excursions that take place between 3 and 12 mm thickness. Referring back to Equation 2.6, the term $\cos 2\beta d$ expresses the effects of coherence and gives rise to damped periodic behavior, such as that observed in Figure 2.3. For each of the multiple frequencies, the phase term (β), and thus the optical path length, changes slightly, implying that the first brightness temperature maximum ($\frac{d}{\lambda_i} = 0.25$) occurs at different physical thicknesses for each frequency. Since the mean thickness was

Table 2.1. Mean ice thicknesses measured at the first maximum $d/\lambda = 0.25$ and first minimum $d/\lambda = 0.50$ in the time series brightness temperature data for each frequency.

Frequency [GHz]	d_o [mm] [$d=\lambda/4$]	d_o [mm] [$d=\lambda/2$]
4.63	5.0	10.5
5.05	4.5	10.0
5.91	4.0	9.0
6.33	4.0	8.0
6.76	3.5	7.5
7.20	3.0	7.0

frequently measured, the SFMR data can be used to estimate the ice dielectric constant.

Table 2.1 presents a list of thicknesses that correspond to the quarter and half wave interference fringes for each of the six frequencies. Using Equation 2.10 and the data presented in Table 2.1, the real part of the dielectric constant of the ice sheet during the early stages of growth was calculated. Results are presented in Figure 2.4, where a linear regression curve is plotted through the data points. Because this calculation is extremely sensitive to errors in thickness measurement, the uncertainty for each point in the plot is approximately ± 2 . The apparent oscillation with frequency is actually an artifact of the accuracy limits of the physical thickness measurements given in Table 2.1. This figure shows that the dielectric constant of ice during the first centimeters of growth is approximately three times larger than the values normally quoted for thick first year ice [7]. Figure 2.5 shows salinity profiles derived from samples collected during the growth of a previous ice sheet.

Note that the salinity is high at the surface, which is a consequence of the significant amount of brine expelled to the surface during the first centimeter of growth. This would explain the extremely high dielectric constant observed radiometrically.

It should be noted that higher order interference fringes are not explicitly evident in the data. There are several possible reasons for this. Inhomogeneities in the dielectric constant may be created by small non-uniform vertical gradients in the salinity profile. Roughness and lateral inhomogeneities of the boundaries may also develop as the ice crystals grow. Any such gradients within the antenna beam would tend to destroy the coherence of the slab. As Swift noted [6], coherence is virtually destroyed when the scale of inhomogeneity is of the order of a quarter wavelength in the dielectric. In our case, a few millimeters of dielectric or roughness variation within the antenna footprint will suffice.

The imaginary part of the index of refraction was also calculated for this sheet according to a procedure developed by Swift [6]. When coherence effects are minimal (as they are in Figure 2.3 for thicknesses greater than 12 mm), the expected value of the emissivity may be approximated as:

$$\langle \epsilon_i \rangle \approx \frac{(1 - r_i)(1 - Ar_{wo})}{(1 - Ar_i)} \quad (2.12)$$

where A and r_i are defined in Equation 2.6, and r_{wo} is the reflection coefficient of water to air. The derivative of Equation 2.12 with respect to frequency is given in the following:

$$\frac{d\langle \epsilon_i \rangle}{df} \approx \frac{(1 - r_i)(r_{wo} - r_i)}{(1 - 2Ar_i + A^2r_i^2)} \frac{8\pi n_i d}{c} \exp\left(\frac{-8\pi n_i f_i d}{c}\right) \quad (2.13)$$

The slope of this function is positive for thin ice and negative for thick ice, indicating that there is a thickness of maximum frequency dependence. Physically, this

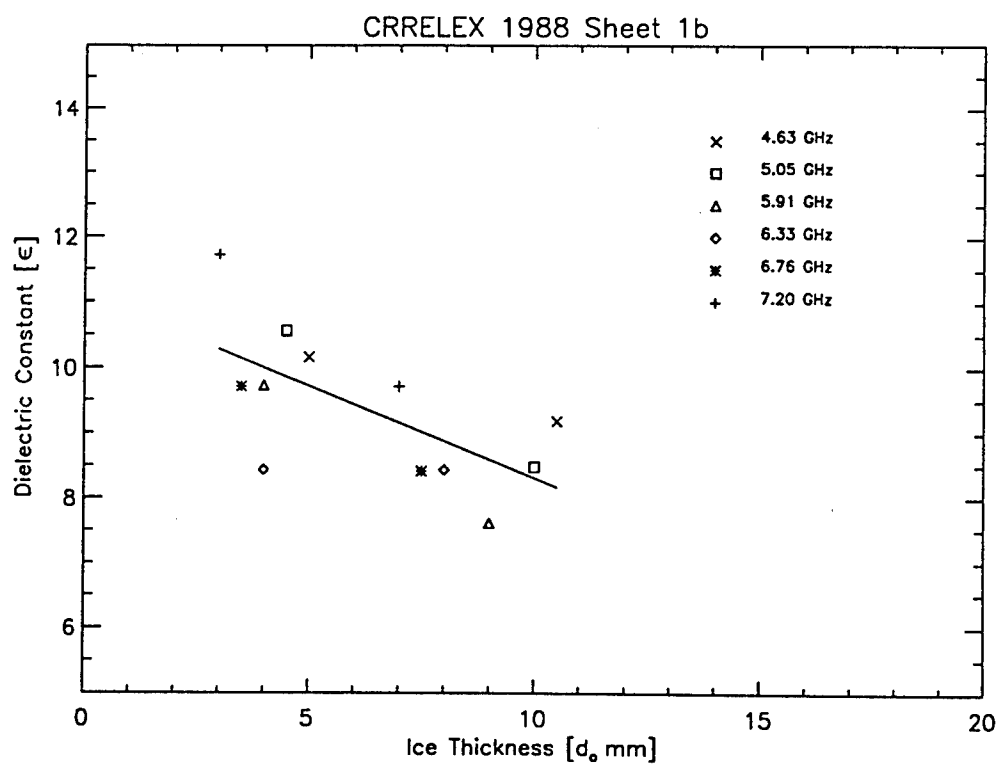


Figure 2.4. Calculated dielectric constant as a function of ice thickness.

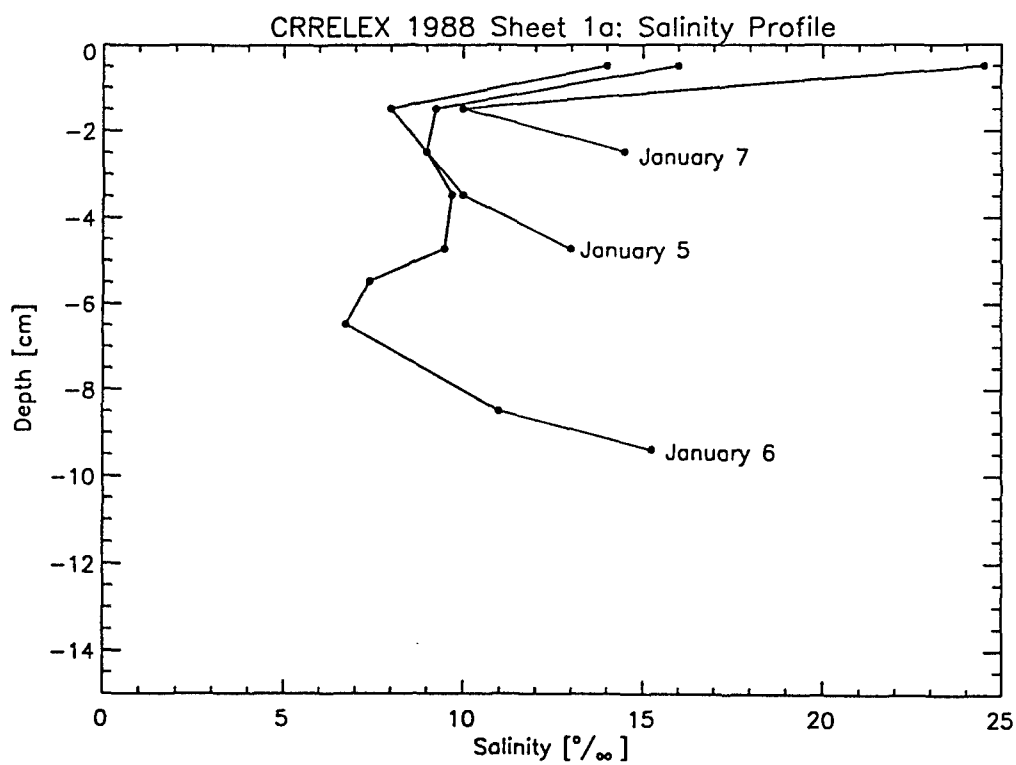


Figure 2.5. Salinity profile of sheet 1A for each day from January 5 through January 7, 1988.

maximum occurs because data collected as a function of frequency tend to merge together when the ice is both very thin and very thick. That is to say, the emission of respective half spaces of ice and water are nearly independent of frequency. The derivative of Equation 2.13 with respect to thickness is zero at this point, yielding the relationship in Equation 2.14.

$$\frac{8\pi n_i f_i d}{c} = 1 \quad (2.14)$$

The thickness of maximum frequency dependency can be estimated from the data, and equation(9) can be solved for n_i . For this sheet, the data show that the thickness of maximum frequency dependence had just been attained when the sheet was harvested, yielding:

$$n_i \approx 0.038 \quad (2.15)$$

which is within range (approximately 0.022 to 0.066) of previously measured C-band values [7]. The previously determined value of the real part of the complex dielectric constant and the imaginary part of the index of refraction may be used to calculate the imaginary part of the dielectric constant, ϵ'' . Equation 2.16 is derived from the definition of index of refraction in terms of complex dielectric constant when the first two terms of the binomial expansion are retained.

$$\epsilon''_i \approx 2\sqrt{\epsilon'_i} n_i \quad (2.16)$$

For this ice sheet, Equation 2.16 yields a value of 0.215 for ϵ''_i , which is also within the range of values reported for similar ice sheets grown at the CRREL facility.

2.2.4 Summary of New Ice Characteristics

As ice forms from open sea water, the magnitude of the surface dielectric constant decreases rapidly from the open water value of 80 to 11 within the first 5mm of growth. It then decreases more slowly to approach a value of 6 as the ice thickness increases to 10cm. With continued growth the dielectric constant will eventually reach the stable first year ice value.

2.3 First Year Ice

Once ice thickness increases past 50 cm, the ice is classified as 'first-year'. At this point the salinity has decreased significantly and the ice may be modeled to first order as a semi-infinite, homogeneous dielectric. The complex dielectric constant is driven by the ice salinity and temperature profile. When the ice temperature is below -10°C , the complex dielectric constant at microwave frequencies is approximately $3.2 - j0.2$ for typical values of salinity, as shown in Figure 2.6. If the air-ice interface is smooth, the solution to the boundary conditions for a plane wave incident at 53° yields vertically polarized emissivity of 0.99 and horizontally polarized emissivity of 0.8. These emissivities are nearly independent of frequency in the microwave portion of the spectrum.

By the time sea ice develops from new ice to the thicker first year ice, it usually has a layer of snow on its surface and the snow-ice interface is no longer smooth. A typical configuration is illustrated in Figure 2.7. The effect of these modifications appears most prominently in the horizontally polarized emissivities, which increase to approximately 0.93 and remain largely independent of frequency.

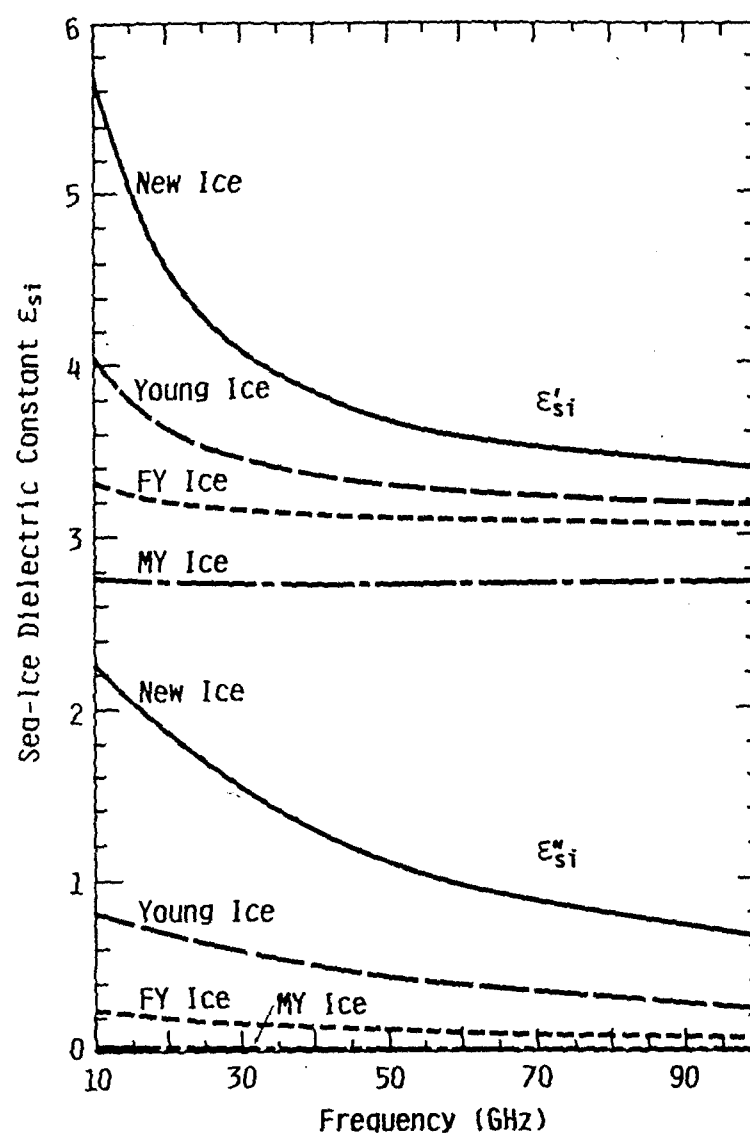


Figure 2.6. Dielectric constant as a function of frequency for first-year ice and multiyear ice. Computed based on typical values of density and dielectric constant [1].

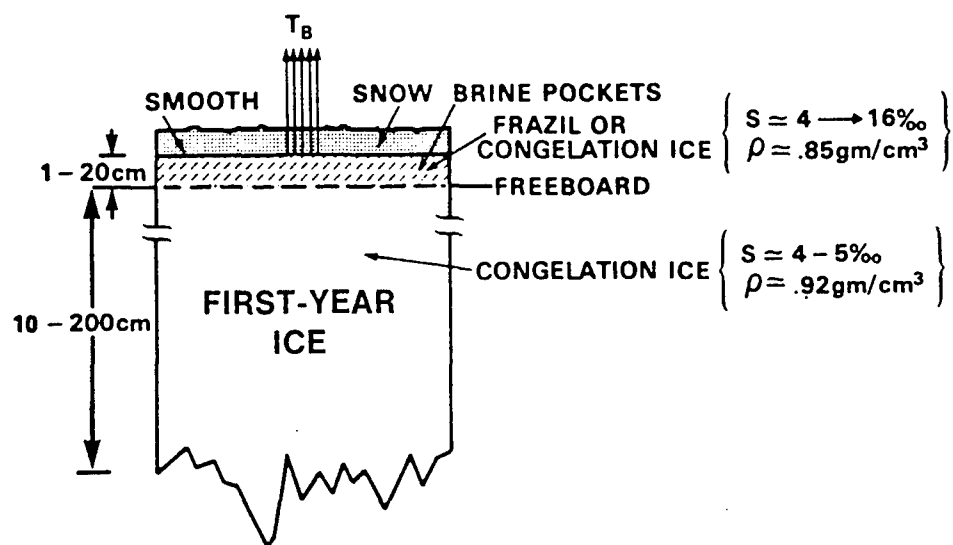


Figure 2.7. Typical geometry for first-year ice [2].

2.4 Multiyear Ice

With the coming of the summer months sea ice in the central Arctic basin suffers some degree of surface melt. In addition, as the ice temperature increases, the brine pockets connect, creating channels. This network of channels forms a mechanism for brine drainage, particularly as the surface melt rinses through the ice.

If the ice survives the summer season, the decreasing temperatures will again cause the ice crystals to grow, pinching off the channels and leaving air pockets in place of the brine. The diameter of these air pockets is typically 1-2mm, which is significant compared to the wavelength at microwave frequencies. Figure 2.8 shows this schematically.

The significant desalination and decrease in density drives the dielectric constant of multiyear ice down to approximately $2.8 - j0.02$, again nearly independent of frequency. Although the real part of the permittivity has changed by only about 10%, the imaginary part has decreased by an order of magnitude. This, again, is a direct result of the drop in conductivity due to the desalination process. The result of this drastic change in conductivity is a marked increase in penetration depth from 2-6cm for first-year ice to 10-20 cm for multiyear ice.

If the emissivity of multiyear ice is calculated using the plane interface approximation that worked so well for first-year ice, the horizontal and vertical emissivities are 0.99 and 0.83 respectively. However, these numbers do not agree at all with the values observed experimentally. Because of the increased penetration depth and the presence of air pockets, multiyear ice must be modeled as a scattering and absorbing medium to reconcile the predicted and observed emissivities.

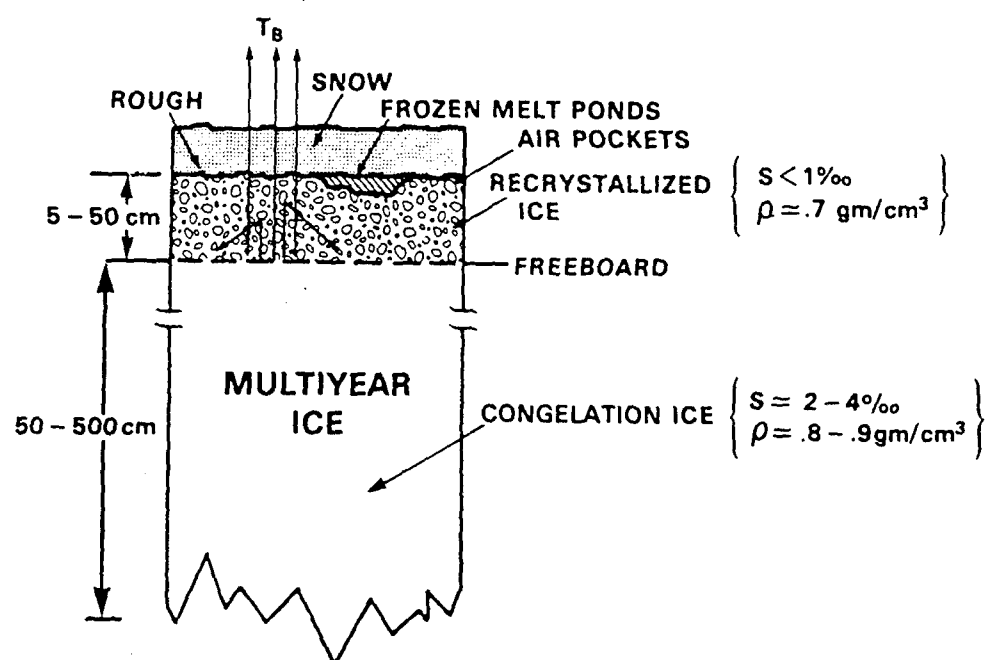


Figure 2.8. Typical geometry for multiyear ice [2].

The scattering coefficient from Equation 2.4 is defined as:

$$\alpha_s = nQ \quad (2.17)$$

- n = Number of scatterers per unit volume
- Q = Scattering cross section of a single scatterer

As Wilheit [2] demonstrates, this approach produces a strong frequency dependence as the single scattering cross section, Q , changes with respect to wavelength. The spectral behavior of multiyear ice emissivity is indicated in Figure 2.9 for nadir viewing. At an off nadir angle of 53° the vertically polarized emissivities increase, while the horizontally polarized emissivities decrease. Finally, if the snow layer and the rough interface are taken into account, the corresponding increase in the horizontally polarized emissivities brings theoretical values into line with measured values.

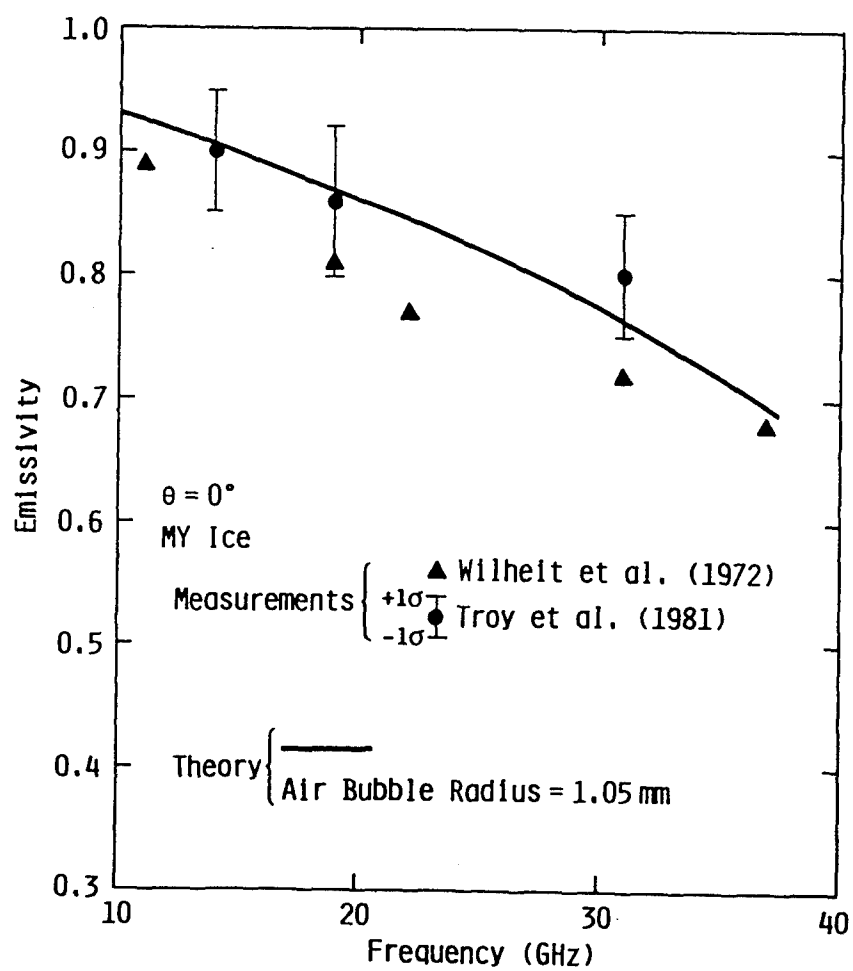


Figure 2.9. Comparison of measured nadir emissivity of multiyear ice with theoretical calculations [2].

CHAPTER 3

EMISSION FROM THE ATMOSPHERE

3.1 Application of Radiative Transfer Theory To The Atmosphere

The microwave brightness temperature of a surface, T_B , depends on the dielectric properties of the material, as discussed in Chapter 2.1, and the physical temperature of the radiating portion of the material. In many cases the permittivity does not change with temperature, and the brightness temperature of the surface can be expressed as:

$$T_B[\lambda, p] = e[\lambda, p]T_s \quad (3.1)$$

where T_B and emissivity, e , are functions of wavelength and polarization for off nadir viewing. Measured brightness temperatures, however, typically contain contributions from several other sources. The relationship between measured T_B and these sources is described by the radiative transfer theory.

The measured microwave brightness temperature of emitted radiation from a surface at some altitude, h , is the sum of the surface brightness temperature measured at the surface, T_{BS} , attenuated by intervening atmosphere, plus the brightness temperature of upwelling atmospheric emission, $T_{B,UP}$:

$$T_B = \tau T_{BS} + T_{B,UP} \quad (3.2)$$

and τ is the transmissivity due to all atmospheric gases, water vapor, clouds, and precipitation. The transmissivity of a particular medium, can be expressed as a

function of the opacity, κ_e (units of nepers, Np) and attenuation or extinction coefficient, α_e (units of Np/km):

$$\kappa = \int_0^z \alpha(z') dz' \quad (3.3)$$

$$\tau = e^{-\kappa} \quad (3.4)$$

The conversion from dB/km to Np/km is simply $\alpha_{Np} = 0.23\alpha_{dB}$.

When the surface is not a perfect absorber, a portion of the downwelling atmospheric emission will be reflected upward. Therefore, when the surface is in thermodynamic equilibrium:

$$T_{BS} = eT_s + (1 - e)T_{DW} \quad (3.5)$$

where T_s is the surface temperature and T_{DW} is the brightness temperature of the downwelling radiation incident at the surface. The term $(1 - e)$ is known as the reflectivity. In terms of transmissivity, downwelling atmospheric radiation, $T_{B,DOWN}$, and cosmic background radiation, T_C , the total downwelling radiation is:

$$T_{DW} = T_{B,DOWN} + \tau T_C \quad (3.6)$$

Combining Equations 3.2, 3.4, 3.5, 3.6, a radiometer at some altitude above the surface will measure radiances according to:

$$T_{B,\lambda,p} = e_{\lambda,p} T_s e^{-\kappa_\lambda} + T_{B,\lambda,Up} + (1 - e_{\lambda,p}) T_{B,\lambda,Down} e^{-\kappa_\lambda} + (1 - e_{\lambda,p}) T_{B,C} e^{-2\kappa_\lambda} \quad (3.7)$$

where the relative contributions are sketched in Figure 3.1 and:

$T_{B,\lambda,p}$	=	measured brightness temperature
$e_{\lambda,p}$	=	total surface emissivity
T_s	=	physical temperature of the radiating portion of the ice
κ	=	atmospheric opacity
$T_{B,\lambda,Up}$	=	total atmospheric upwelling radiation
$T_{B,\lambda,Down}$	=	total atmospheric downwelling radiation
$T_{B,C}$	=	cosmic background radiation, 2.7 Kelvin at microwave frequencies

The upwelling and downwelling atmospheric radiation can be approximated as:

$$T_{ATM} = \langle T \rangle (1 - e^{-\kappa_\lambda}) \quad (3.8)$$

where $\langle T \rangle$ is a constant weighted average atmospheric temperature and $e^{-\kappa_\lambda}$ represents total atmospheric loss. A detailed development of this approximation is included in Section 3.1.1.

The atmospheric parameters in Equation 3.7 depend strongly on such variables as atmospheric pressure, temperature, and vapor profiles. These profiles and the corresponding atmospheric effects vary tremendously from the tropical to the polar regions. Since T_{ATM} and κ are integrated parameters, they also contain a significant dependence on radiometer altitude. For instance, downward looking ground based instruments will see little effect from the second term in Equation 3.7, and for surface emissivity close to 1.0, the same may be true of the third and fourth terms. Conversely, at typical aircraft altitude in the tropics, all terms must be maintained and modeled. This case is addressed in the following section. Finally, at typical satellite altitudes in the Arctic, the atmospheric contribution is small, but not always negligible as Section 3.1.2 demonstrates.

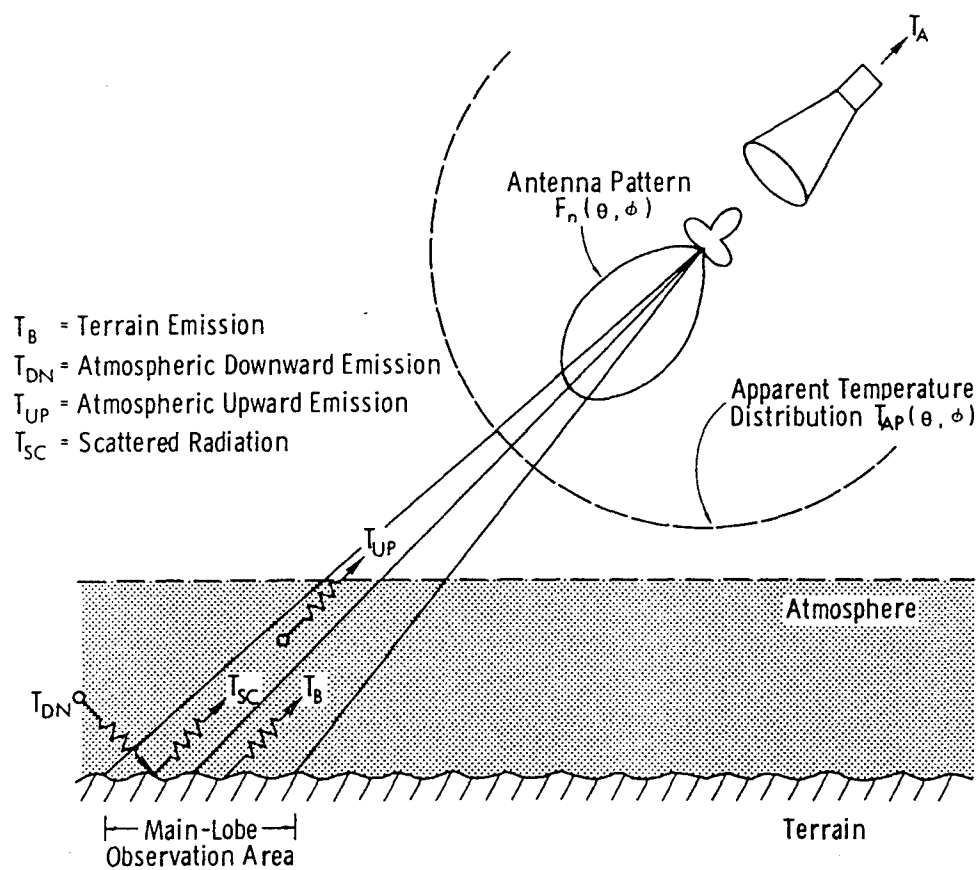


Figure 3.1. Schematic representation of the radiative transfer equation [1].

3.1.1 Microwave Brightness Temperature Equation in a tropical hurricane case study

Passive microwave radiometry has been used to estimate rainrate and ocean surface windspeed in hurricanes. The following discussion presents the geophysical variables that drive both the surface and atmospheric terms in the radiative transfer equation.

To tailor Equation 3.7 to a tropical hurricane application, several geophysical variables must be incorporated. The transmissivity τ can be expressed as the product of the transmissivity of rain and the transmissivity of atmospheric gases. Since the measurements are made from an aircraft, τ must be defined for both the entire atmospheric column and the column below the aircraft altitude h . Equation 3.6 then becomes:

$$T_{DW} = T_{Dh} + \tau_a \tau_r T_{DH} + \tau_A \tau_R T_C \quad (3.9)$$

where τ_A and τ_R are the atmospheric gas and rain transmissivities for the entire atmosphere and rain column, respectively. τ_a and τ_r are the corresponding values for the layer below h . T_{Dh} and T_{DH} represent the total downwelling atmospheric radiation temperature from the regions below and above the flight altitude, respectively. According to Ulaby et al., [1], the brightness temperature of the radiation emitted from an atmospheric layer cannot be approximated as in Equation 3.8, but must be expressed as a function of the temperature and attenuation coefficient of emitting gases or particles:

$$T_{ATM} = \int_0^z T(z') \alpha(z') e^{-\int_0^{z'} \alpha(z'') dz''} dz' \quad (3.10)$$

The effective temperature of the atmosphere, $\langle T \rangle$, which is the attenuation weighted, column-averaged air temperature can now be defined as :

$$\langle T \rangle = \frac{\int_0^z T(z') \alpha(z') e^{-\int_0^{z'} \alpha(z'') dz''} dz'}{\int_0^z \alpha(z') e^{-\int_0^{z'} \alpha(z'') dz''} dz'} \quad (3.11)$$

Therefore,

$$T_B = \langle T \rangle \int_0^z \alpha(z') e^{-\int_0^{z'} \alpha(z'') dz''} dz' \quad (3.12)$$

The effective temperature, $\langle T \rangle$, is indicated by $\langle T_a \rangle$ for atmospheric gas attenuation weighted air temperature or $\langle T_r \rangle$ for rain attenuation weighted air. The limit of integration, z , is the aircraft altitude, h or the rain depth equal to or smaller than h . When the limit of integration is the top of the atmosphere or the rain depth is larger than h , the upper case subscripts are used. Expressing the above in terms of the opacity, κ , as defined earlier:

$$T_B = \langle T \rangle (1 - \tau_e) \quad (3.13)$$

T_{Dh} and T_{DH} are expressed in integral form according to:

$$T_{Dh} = \int_0^h [\alpha_R(z) + \alpha_A(z)] T(z) e^{-\int_0^z [\alpha_R(z') + \alpha_A(z')] dz'} dz \quad (3.14)$$

$$T_{DH} = \int_h^\infty [\alpha_R(z) + \alpha_A(z)] T(z) e^{-\int_h^z [\alpha_R(z') + \alpha_A(z')] dz'} dz \quad (3.15)$$

The downwelled radiation temperature from the atmosphere above h , T_{DH} , can be expressed as the difference between two integrals:

$$T_{DH} = \int_h^\infty [\alpha_R(z) + \alpha_A(z)] T(z) e^{-\int_0^z [\alpha_R(z') + \alpha_A(z')] dz'} + \int_0^h [\alpha_R(z') + \alpha_A(z')] dz' dz$$

$$\begin{aligned}
T_{DH} = & \int_0^\infty [\alpha_R(z) + \alpha_A(z)] T(z) e^{-\int_0^z [\alpha_R(z') + \alpha_A(z')] dz' + \int_0^h [\alpha_R(z') + \alpha_A(z')] dz'} dz \\
& - \int_0^h [\alpha_R(z) + \alpha_A(z)] T(z) e^{-\int_0^z [\alpha_R(z') + \alpha_A(z')] dz' + \int_0^h [\alpha_R(z') + \alpha_A(z')] dz'} dz
\end{aligned} \tag{3.16}$$

Integrating and expressing the result in terms of transmissivities and effective temperatures gives:

$$T_{Dh} = \tau_r \langle T_a \rangle (1 - \tau_a) + \tau_a \langle T_r \rangle (1 - \tau_r) \tag{3.17}$$

At this point, the braces denoting effective temperature will be dropped:

$$T_{DH} = \tau_a^{-1} \tau_r^{-1} [\tau_r T_A (1 - \tau_A) + \tau_A T_R (1 - \tau_R) - \tau_r T_a (1 - \tau_a) - \tau_a T_r (1 - \tau_r)] \tag{3.18}$$

Collecting terms, the downwelling temperature then becomes:

$$T_{DW} = \tau_R T_{DWC} + \tau_A T_R (1 - \tau_R) \tag{3.19}$$

where

$$T_{DWC} = T_{SKY} + (1 - \tau_a) T_A \tag{3.20}$$

is the clear sky downwelling temperature incident on the sea surface and

$$T_{SKY} = \tau_A T_C \tag{3.21}$$

is the sky temperature contribution at the sea surface from the cosmic background radiation. Collecting terms further:

$$T_{DW} = \tau_R \rho + \tau_A T_R \tag{3.22}$$

where

$$\rho = T_{DWC} - \tau_A T_R \tag{3.23}$$

The upward radiating brightness temperature of the sea, T_{BS} , can now be written as:

$$T_{BS} = \epsilon T_S + (1 - \epsilon)(\tau_R \rho + \tau_A T_R) \quad (3.24)$$

To calculate the brightness temperature that the radiometer "sees" at level h , the brightness temperature of the upward emission from the atmosphere (gases and rain) below the aircraft, T_{BA} , must be estimated:

$$T_{BA} = \int_0^h [\alpha_R(z) + \alpha_A(z)] T(z) e^{-\int_z^h [\alpha_R(z') + \alpha_A(z')] dz'} dz \quad (3.25)$$

Expressing the exponential as the difference between two integrals,:

$$T_{BA} = \int_0^h [\alpha_R(z) + \alpha_A(z)] T(z) e^{-\int_0^h [\alpha_R(z') + \alpha_A(z')] dz' + \int_0^z [\alpha_R(z') + \alpha_A(z')] dz'} dz \quad (3.26)$$

Integrating and expressing the result in terms of transmissivities as before, produces:

$$T_{BA} = (1 - \tau_a) T_a + (1 - \tau_r) T_r \quad (3.27)$$

Making the simplifying assumption that $T_a = T_r = T_e$, typical values of τ_r and τ_a yield:

$$T_{BA} \approx (1 - \tau_a \tau_r) T_e \quad (3.28)$$

The measured brightness temperature at flight level T_B then becomes:

$$T_B = \tau_a \tau_r \epsilon T_S + \tau_a \tau_r (1 - \epsilon) T_{DW} + (1 - \tau_a \tau_r) T_e \quad (3.29)$$

The emissivity of the sea surface, ϵ , is a function of frequency and foam coverage. The amount of foam (entrained air bubbles in the water) on the sea surface is a function of wind speed and sea temperature (to a second order, which will be ignored here). Expressing the surface emissivity in terms of a smooth water emissivity that

is a function only of frequency, $\mu(f)$, and rough surface emissivity that is the product of two terms: $\gamma(U)$, which is a function of surface wind speed and $L(f)$, which is a function of frequency. Therefore,

$$\epsilon(U, f) = L(f)\gamma(U) + \mu(f) \quad (3.30)$$

The brightness temperature equation thus becomes:

$$T_B - T_e = \tau_a \tau_r [(1 - \mu)T_{DW} + \mu T_s - T_e] + \gamma L \tau_a \tau_r (T_s - T_{DW}) \quad (3.31)$$

Finally one must relate τ_r , τ_a , and γ to geophysical variables. Typically this is done empirically. Once these relationships are established, brightness temperature measurements at several frequencies are used to solve Equation 3.31 for windspeed and rainrate. An inversion algorithm, along with the details of the relationship between τ_a , τ_r and γ and atmospheric gases, rainrate and windspeed are discussed in Appendix I.

3.1.2 Microwave Brightness Temperature Equation in a polar case study

Because the temperature and humidity are normally low in the high Arctic, the atmosphere normally contributes little to brightness temperature measurements at most microwave frequencies. This is particularly true over pack ice where the surface emissivity is close to one. However, in the marginal ice zone, vapor, clouds, and precipitation are common, and the radiometrically cool surface of open water enhances atmospheric effects on brightness temperature.

When measurements are made from a satellite, the form of the radiative transfer equation is much simpler than in the aircraft measurements described in the previous section. It is only necessary to account for integrated atmospheric values of vapor,

cloud liquid water, and oxygen. Accordingly the opacity κ may be approximated by:

$$\kappa = \kappa_{VAP} + \kappa_{LIQ} + \kappa_{O_2} \quad (3.32)$$

$$\kappa_{VAP} = AV \quad (3.33)$$

$$\kappa_{LIQ} = BL \quad (3.34)$$

$$\kappa_{O_2} = C \quad (3.35)$$

where:

- V = Total integrated atmospheric vapor
- L = Total integrated cloud liquid water
- A = Frequency and temperature dependent coefficient linearly relating integrated vapor to opacity
- B = Frequency and temperature dependent coefficient linearly relating integrated cloud liquid water to opacity
- C = Frequency dependent opacity due to oxygen

The coefficients and the total upwelling and downwelling atmospheric brightness temperatures were determined in the following manner. The oxygen, vapor, and liquid water absorption coefficients are expressed in terms of ambient temperature, atmospheric pressure, water vapor volume density, and frequency according to [1].

$$\kappa_{H_2O}(f) = 2f^2 \rho_v \left(\frac{300}{T}\right)^{\frac{3}{2}} \gamma_1 \left[\frac{300}{T} e^{\frac{644}{T}} \frac{1}{(494.4 - f^2)^2 + 4f^2 \gamma^2} + 1.2 \times 10^{-6} \right] \text{dBkm}^{-1} \quad (3.36)$$

where

$$\gamma_1 = 2.85 \left(\frac{P}{1013}\right) \left(\frac{300}{T}\right)^{0.626} \left[1 + 0.018 \frac{\rho_v T}{P}\right] \text{GHz} \quad (3.37)$$

For measurements below 45 GHz, the contribution of the 60 GHz oxygen resonance complex may be estimated as:

$$\kappa_{O_2}(f) = 1.1 \times 10^{-2} f^2 \left(\frac{P}{1013} \right) \left(\frac{300}{T} \right)^2 \times \gamma \left[\frac{1}{(f - f_o)^2 + \gamma^2} + \frac{1}{f^2 + \gamma^2} \right] \text{dBkm}^{-1} \quad (3.38)$$

The linewidth parameter γ is

$$\gamma = \gamma_o \left(\frac{P}{1013} \right) \left(\frac{300}{T} \right)^{0.085} \text{GHz} \quad (3.39)$$

$$\begin{array}{llll} \gamma_o & = & 0.59 & P \geq 333 \text{ mbar} \\ & = & 0.59[1 + 3.1 \times 10^{-3} (333 - P)] & 25 \leq P \leq 333 \text{ mbar} \\ & = & 1.18 & P \leq 25 \text{ mbar} \end{array}$$

Temperature and air density profiles for Arctic atmosphere are available from climatology studies [4], and are included here for convenience.

$$\begin{array}{llll} T(z) & = & T_{SURF} + 0.002575z & z < 1670\text{m} \\ & = & T_{SURF} + 4.3 - 0.00541 (z - 1670) & 1670\text{m} \leq z \leq 8000\text{m} \\ & = & T_{SURF} - 30.0 & 8000\text{m} < z \end{array}$$

$$\rho_{AIR}(z) = \frac{e^{-0.127 \left(\frac{z-5719}{1000} \right)}}{1000} \quad (3.40)$$

Substituting Equation 3.36 and the above profiles into Equations 3.3, 3.4, 3.12 and integrating through the atmospheric column for a range of values of surface temperature and vapor yields the following relationship for coefficients A in Equation 3.32:

$$A_{19} = \frac{2.1 + 0.0005T_s}{1000} \quad (3.41)$$

$$A_{22} = \frac{17.8 + 0.013T_s}{1000} \quad (3.42)$$

$$A_{37} = \frac{4.4 - 0.0093T_s}{1000} \quad (3.43)$$

A similar analysis for cloud liquid water coefficients gives:

$$B_{19} = \frac{89.7 - 0.263T_s}{100} \quad (3.44)$$

$$B_{22} = \frac{90.7 - 0.264T_s}{100} \quad (3.45)$$

$$B_{37} = \frac{298.4 - 0.903T_s}{100} \quad (3.46)$$

Finally, since atmospheric oxygen is considered known, the total atmospheric attenuation due to oxygen is expressed in the C coefficients:

$$C_{19} = \frac{2.69 - 0.0057T_s}{100} N_p \quad (3.47)$$

$$C_{22} = \frac{2.96 - 0.0063T_s}{100} N_p \quad (3.48)$$

$$C_{37} = \frac{7.95 - 0.0167T_s}{100} N_p \quad (3.49)$$

These relationships are used in the Weather Correcting Decision Algorithm presented in Section 4.3.

For most of the central Arctic it is reasonable to assume that the atmosphere is saturated with vapor but contains negligible cloud liquid water. Under these conditions opacity may be computed as a function only of T_s the atmospheric attenuation due to water vapor is

$$\kappa_{VAP_{19}} = \frac{e^{0.0878(T_s - 225.8)}}{1000} N_p \quad (3.50)$$

$$\kappa_{VAP_{22}} = \frac{e^{0.0864(T_s - 198.8)}}{1000} N_p \quad (3.51)$$

$$\kappa_{VAP_{37}} = \frac{e^{0.0851(T_s - 224.2)}}{1000} N_p \quad (3.52)$$

and the weighted average atmospheric temperature in Equation 3.8 is

$$\langle T \rangle_{19} = -27.5 + 1.08T_s \quad (3.53)$$

$$\langle T \rangle_{22} = 10.0 + 0.91T_s \quad (3.54)$$

$$\langle T \rangle_{37} = -23.0 + 1.06T_s \quad (3.55)$$

This summarizes the approximations made in Section 4.2.

CHAPTER 4

SSM/I ALGORITHMS

4.1 Review of Previous and Current Algorithms

4.1.1 Ice Type and Concentration

Surface type is the most important of the environmental variables that contribute to microwave signatures in the polar regions. At microwave frequencies consolidated sea ice, which appears radiometrically warm, contrasts powerfully with open water, which appears radiometrically cool. The Electronically Steered Microwave Radiometer (ESMR), launched in 1972, exploited this to estimate the relative amounts of ice and water within the 100 km footprint of the instrument. The estimates were based on a simple linear relationship between the open water and pack ice brightness temperatures. It was discovered, however, that the brightness of desalinated multiyear ice lies in between the open water and first-year ice values. For the single frequency ESMR system this produced unavoidable ambiguities in the estimated ice concentrations.

As Chapter 2.4 explains, volume scattering in the upper portion of multiyear ice, makes its spectral behavior quite different from both water and first-year ice. This was discussed in detail in Chapter 3.1. When the Scanning Multichannel Microwave Radiometer (SMMR) instruments were launched in 1978, the ten channels (6.6, 10.7, 18.0, 21.0, and 37 GHz, vertical and horizontal polarization) offered the opportunity

to identify ice type as well as total concentration. However, the transitional surface types, namely thin ice and second year ice, are not commonly identified and are assumed to contribute small errors to type and concentration estimates.

Several algorithms were proposed to accomplish the task of resolving ice concentration and type from the SMMR data. The two primary contenders were the UMASS/AES algorithm, which was developed jointly by the University of Massachusetts and the AES, and NASA Team algorithms. Each involved simplifications to the radiative transfer equation, with the major difference being the treatment of surface temperature.

The UMASS/AES algorithm required an externally input estimate of surface temperature, accurate to better than ± 10 for retrieval accuracies of $\pm 5\%$. The Team algorithm avoided the issue of surface temperature by forming two ratios which are largely independent of temperature. The polarization ratio,

$$PR = \frac{Tb_{37V} - Tb_{37H}}{Tb_{37V} + Tb_{37H}} \quad (4.1)$$

and the gradient ratio,

$$GR = \frac{Tb_{37V} - Tb_{19V}}{Tb_{37V} + Tb_{19V}} \quad (4.2)$$

are two independent variables. With knowledge of pure ice type tie points, the relative concentrations of first-year ice, multiyear ice, and water may be estimated from the two ratios. Although the UMASS/AES algorithm was deemed less sensitive to instrument noise, the Team algorithm was selected to become the operational algorithm because of its temperature independence.

4.1.2 Ice Temperature

Those studying global climatology, hydrology, and biology need to know the surface temperature of the polar regions. In the Arctic this information has been inferred from data gathered by buoys drifting on ice floes [16]. The considerable difficulties of this method have encouraged the remote sensing community to develop alternatives. Satellite based infrared sensors such as Advanced Very High Resolution Radiometer (AVHRR) offer greater Arctic coverage and high resolution, but information retrieval is seriously constrained by cloud cover contamination. Satellite based passive microwave instruments solve this problem, but at the cost of ground spatial resolution.

Realizing this, Gloersen et al. began producing ice temperature as a secondary product. The SMMR radiances were used to calculate sea ice temperature for the nine year lifespan of the instrument. When the sensor footprint is filled primarily by first year ice, the retrieved temperature is expected to represent the physical temperature of the snow-ice interface because the majority of the microwave emission originates from this region. In contrast, when the scene is composed entirely of multiyear ice, the temperature represents the layer of ice at the bottom of the freeboard layer, just above sea level. Comparisons of retrieved temperature from passive microwave data with ground truth data sets yields encouraging results, particularly during the winter months.

The SMMR ice temperature algorithm makes use of the first order relationship between brightness temperature and physical temperature of an emitting medium:

$$Tb = e(\lambda, p) * T_{ice} \quad (4.3)$$

In the case of sea ice, emissivity is nearly independent of physical temperature (below -12°C) and thus if the ice concentration within the footprint is known from and ice concentration algorithm, the physical temperature of the ice may easily be calculated according to:

$$T_{ice} = \frac{Tb_{6.6v_{obs}} - (1 - C)Tb_{6.6v_{water}}}{e_{6.6v}C} \quad (4.4)$$

The emissivity is estimated based on a combination of infrared and SMMR radiances. It should also be noted that when the ice concentration, C , is eighty percent or less, T_{ice} is set to 271K.

A comparison of wintertime (7-month) ice temperature from SMMR and Arctic Ocean Buoy Program (AOBP) data showed that a linear relationship exists between the two temperatures. A linear least-squares fit yields a slope of 0.5 and an offset of -3.5K. The standard error of estimate is 4.7K, and the correlation coefficient is 0.6. Conclusions drawn from this comparison are limited by inherent differences between the measurements. For example, the AOBP temperature represent point measurements at a fixed depth, whereas the SMMR derived temperatures are interpreted as a spatial average at a depth that is a function of primarily of ice type and snow cover. In addition, the buoy data may be contaminated by drifting snow, solar heating, or faulty operation. In general, the warmer SMMR temperatures are consistent with the subsurface nature of the microwave radiation and the trends indicated by the buoy data are represented in the SMMR results.

4.2 Modification to the NASA Team Algorithm

4.2.1 Algorithm Description

Although the NASA-Team algorithm was developed to interpret SMMR data in the polar regions, it was later modified and applied to data from the DMSP SSM/I as well. This was possible because most of the SSM/I channels are close in frequency to the SMMR channels. The SMMR temperature algorithm could not be used, however, because SSM/I lacked the 4.6cm channel.

Following the lead of Gloersen et al, a modification to the SSM/I Team algorithm was developed to investigate the possibility of extracting temperature product from the SSM/I passive microwave data. This addition to the NASA-Team algorithm requires estimates of ice emissivity as a function of frequency and ice type, and a model of the Arctic atmosphere as function of surface temperature (assuming near vapor saturation).

The basic principle of operation is similar to the NASA-Team temperature algorithm, with the exceptions that ice type distinctions are made and the higher frequency channels are used. To reduce uncertainties introduced by atmospheric vapor, a model of atmospheric opacity was developed. This model was described in detail in Section 3.1.2. Neglecting the small contribution from the reflected terms in Equation 3.7, the inclusion of an atmosphere model produces the following equation:

$$T_B = e_{tot}T_s e^{-\kappa} + T_{atm}(1 - e^{-\kappa}) \quad (4.5)$$

Table 4.1. Emissivity tie points used in the modification to the SSM/I team algorithm.

Surface	Frequency and Polarization		
	19 GHz V	19 GHz H	37 GHz V
First-year	.999	.941	.979
Multiyear	.918	.839	.766
Water	.653	.371	.742

where:

- T_B = measured brightness temperature
- e_{TOT} = total surface emissivity based on retrieved ice concentrations and emissivity tie points
- T_{ATM} = weighted atmospheric temperature as a function of T_s
- κ = atmospheric attenuation coefficient as a function of T_s

The total surface emissivity e_{TOT} is estimated using the concentration estimates from the NASA algorithm and the emissivity tie points presented in Table 4.1. For each frequency, T_B is measured leaving T_s as the only unknown. Because of the dependence of κ on T_s , Equation 4.5 cannot be solved directly, so an iterative routine is employed.

The routine begins with a first guess value for surface temperature and calculates an expected T_{Bexp} for each frequency. These values are then compared with the actual measured brightness temperatures, and the next guess at surface temperature is adjusted accordingly. This routine typically converges in three iterations over the ice pack.

4.2.2 Temperature Evaluation

For obvious reasons reliable ground truth data is rare in the polar regions. Expeditions are few and usually take place during the spring and summer, rarely venturing to the central Arctic basin. One potential source of surface information is the Arctic Ocean Buoy Program (AOPB), which monitors several buoys drifting freely on ice floes throughout the Arctic. These buoys supply hourly temperature measurements along with drift velocity, windspeed, and several other meteorological parameters. There has been much debate about the accuracy of the temperature measurements, largely because of snow drift, greenhouse warming of the enclosure, and other environmental conditions. An additional concern is the difference in spatial scale between a 'point' buoy measurement and the 25 km² resolution of the SSM/I Grid.

With these limitations in mind, the algorithm-derived temperatures and buoy temperatures supplied by the Polar Science Center at the University of Washington were compared. The data set is comprised of temperatures from eight buoys for every odd day in March, 1988. Figure 4.1 is a cluster plot of the algorithm temperatures versus the buoy temperatures. The correlation coefficient is 0.731, and a linear regression yields a slope of 1.06, an offset of 24.56, and an RMS difference between the temperatures of 4.87K. Although this comparison is encouraging, it is far from conclusive.

To overcome the problem of spatial scale, other remote sensing data were investigated. In 1991, the Naval Oceanographic and Atmospheric Research Laboratory (NOARL) Remote Sensing Branch released an Advanced Very High Resolution Radiometer (AVHRR) data set for the Arctic Leads Accelerated Research Initiative

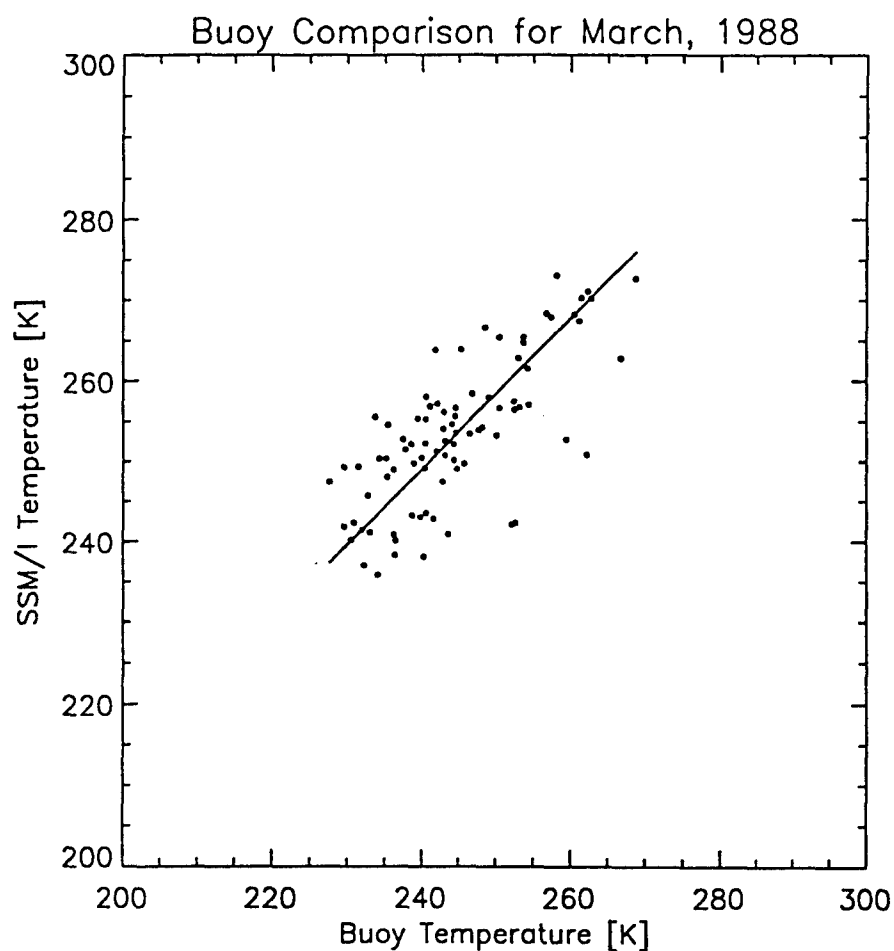


Figure 4.1. Temperature derived from the modified Team algorithm versus buoy temperatures supplied by the Arctic Ocean Buoy Program. The data set includes data from all operational buoys for every odd day in March, 1988

(Arctic Leads ARI) [3]. Although AVHRR data had been available for some time, it was prohibitively difficult to calibrate and geolocate. The data set produced by NOARL is calibrated and mapped to a stereographic projection identical to that used for the gridded Arctic SSM/I data. Since the AVHRR resolution is one square kilometer, 2 grids are required to cover the Arctic region. These grids are shown in Figure 4.2.

As part of an ongoing project at the Applied Physics Laboratory, University of Washington, a temperature product was produced from the gridded AVHRR data. The cloud-masked AVHRR data was processed using an algorithm recently proposed by Key and Haeffiger [17]. The algorithm operates on the three thermal infrared channels (channels 3,4, and 5 centered at 3.7, 11, and 12 μm respectively) available from the AVHRRs aboard NOAA 7,9, and 11. Figure 4.3 represents one of the thirteen 512 Km^2 temperature images used.

To facilitate an intercomparison, the 1 Km^2 AVHRR resolution had to be degraded to match that of the SSM/I polar grid. The AVHRR image with resolution degraded to 25 Km^2 is shown in Figure 4.4, and the corresponding SSM/I derived temperatures are presented in Figure 4.5. Because daily averaged SSM/I data was used, no effort to correlate the time of overpass was made. The cluster plot for this comparison appears in Figure 4.6, and the cluster plot for the entire thirteen day study is presented in Figure 4.7. A regression analysis was performed on each of these plots that minimized the perpendicular distance from each point to the fit, as opposed to the standard Y on X regression. The regression slope for Figure 4.7 is 2.04, while the correlation coefficient is 0.848 and the RMS difference from the fit is 1.57K.

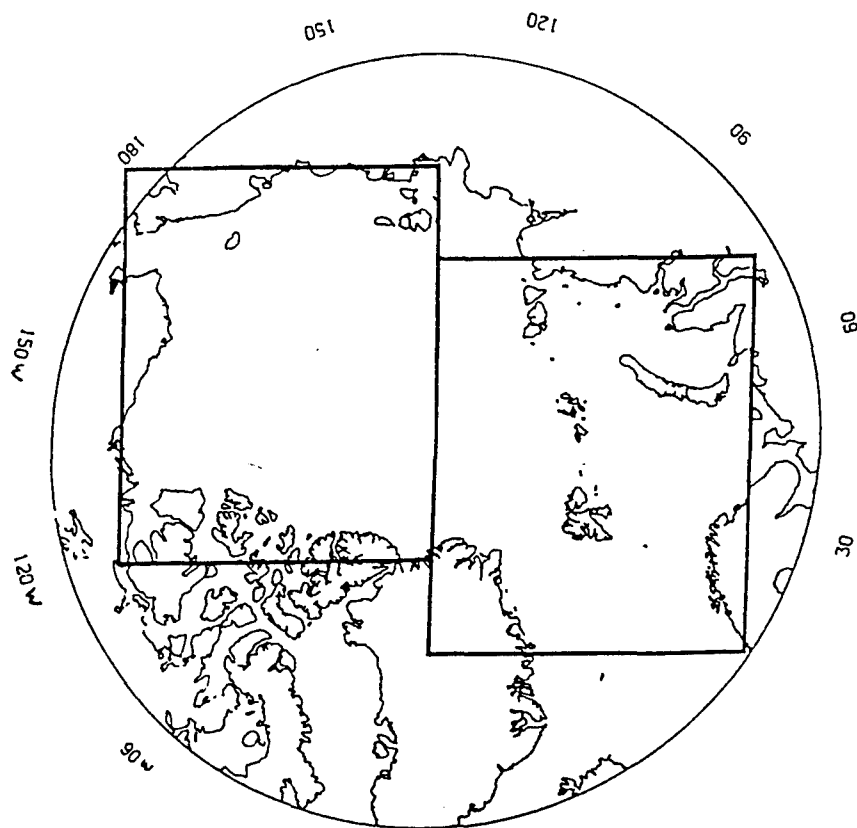
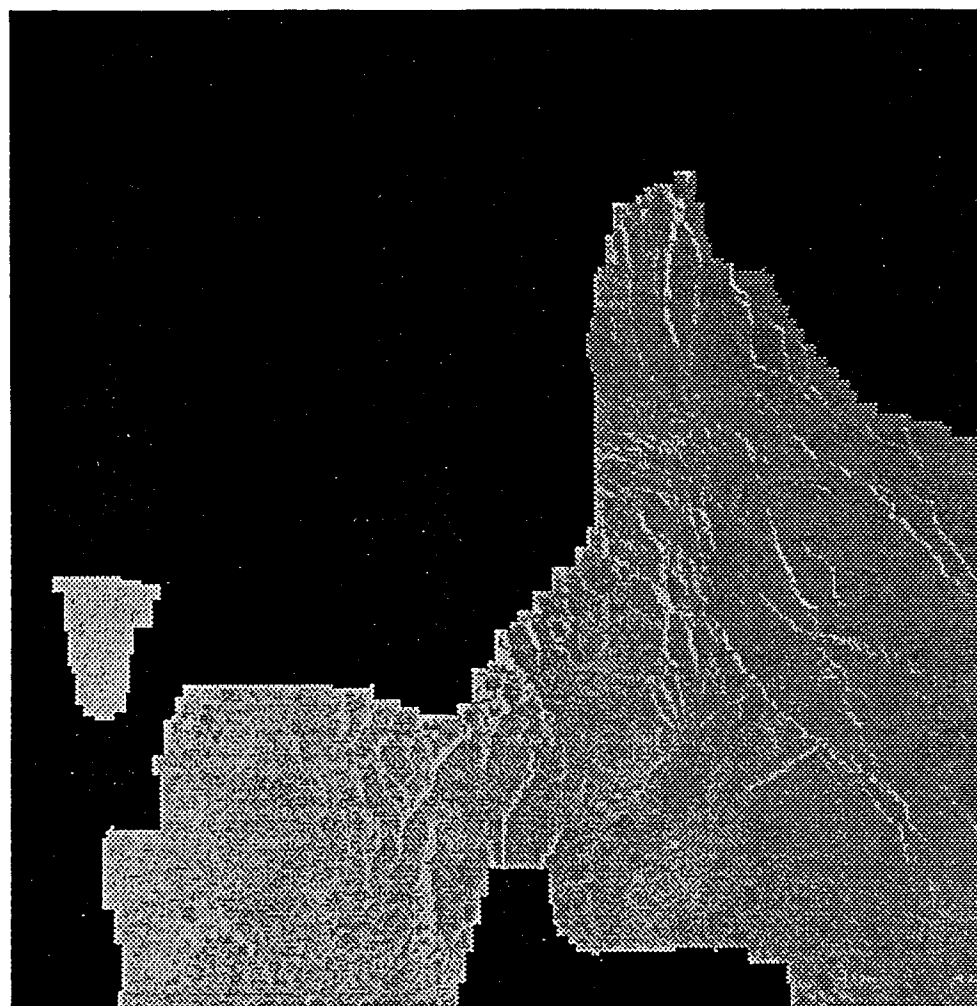


Figure 4.2. AVHRR Arctic Grids. Identified as 'Pacific' and 'European', the grids have 1 Km² resolution [3].



March 17, 1989 – 1,512 P
AVHRR Ice Temperature (K)

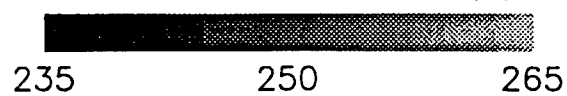
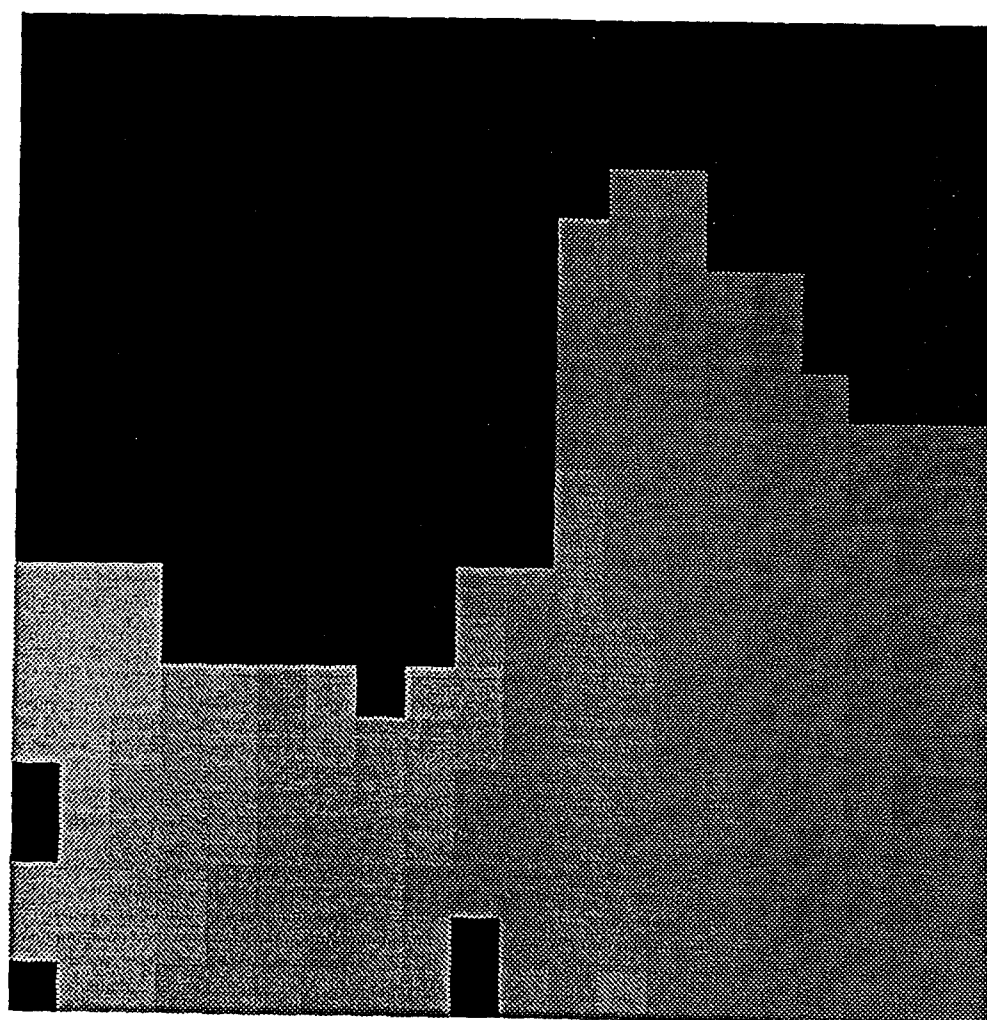


Figure 4.3. Ice/snow surface temperature derived from the AVHRR thermal channels. Black area is masked for clouds.



March 17, 1989 – 1,512 P
AVHRR Averaged Ice Temperature (K)

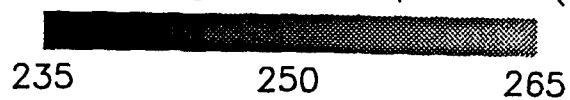
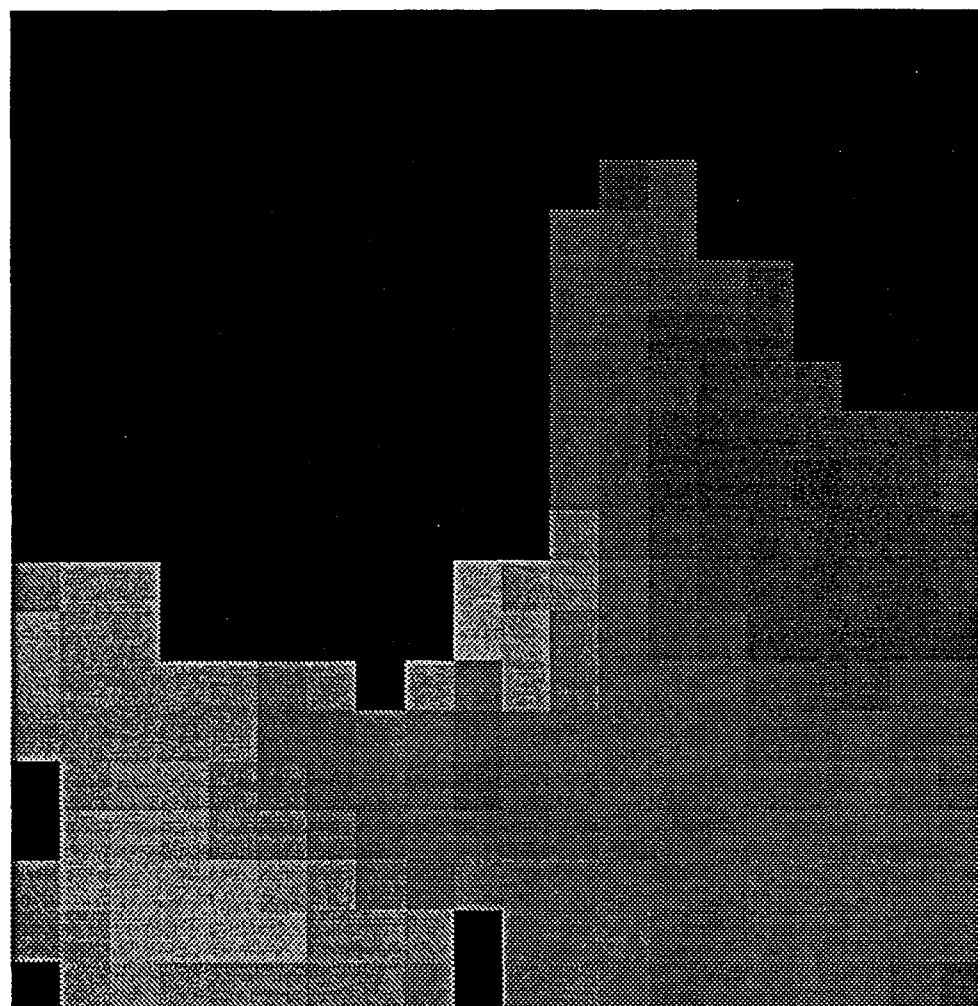


Figure 4.4. AVHRR temperatures degraded to the 25 Km² resolution of the SSM/I polar grid.



March 17, 1989 - 1,512 P
SSM/I Ice Temperature (K)

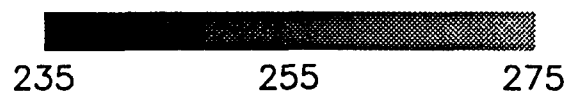


Figure 4.5. SSM/I derived temperatures corresponding to the AVHRR image in Figure 4.3

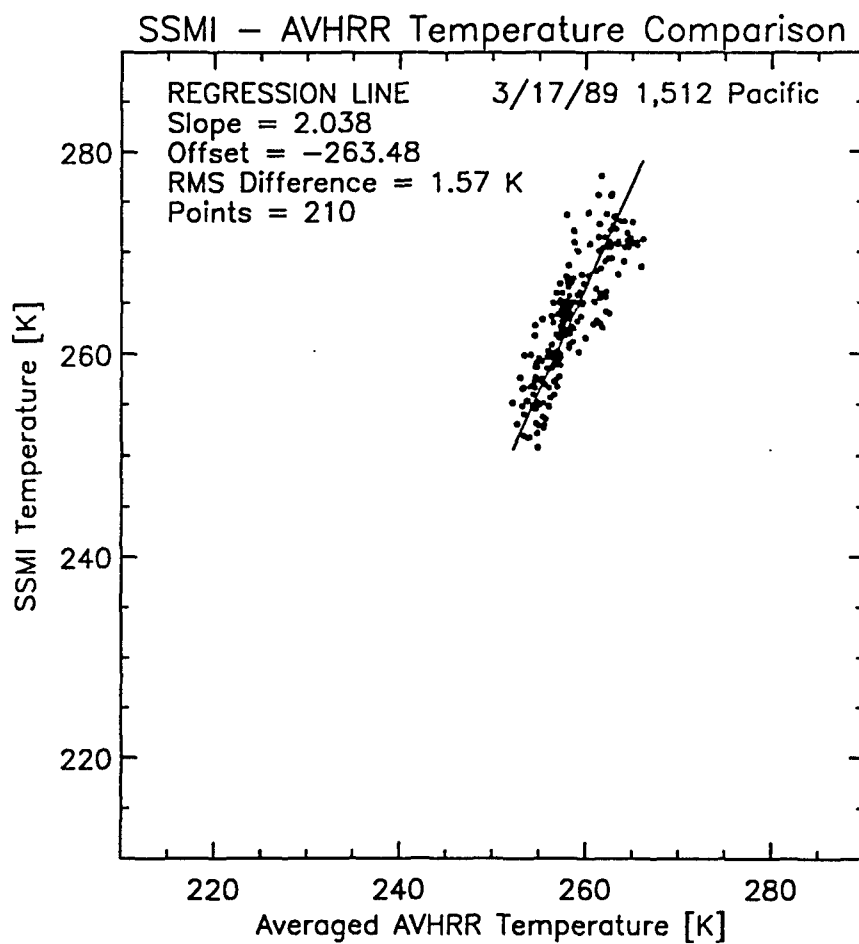


Figure 4.6. Cluster plot corresponding to the temperatures presented in Figures 4.4 and 4.5.

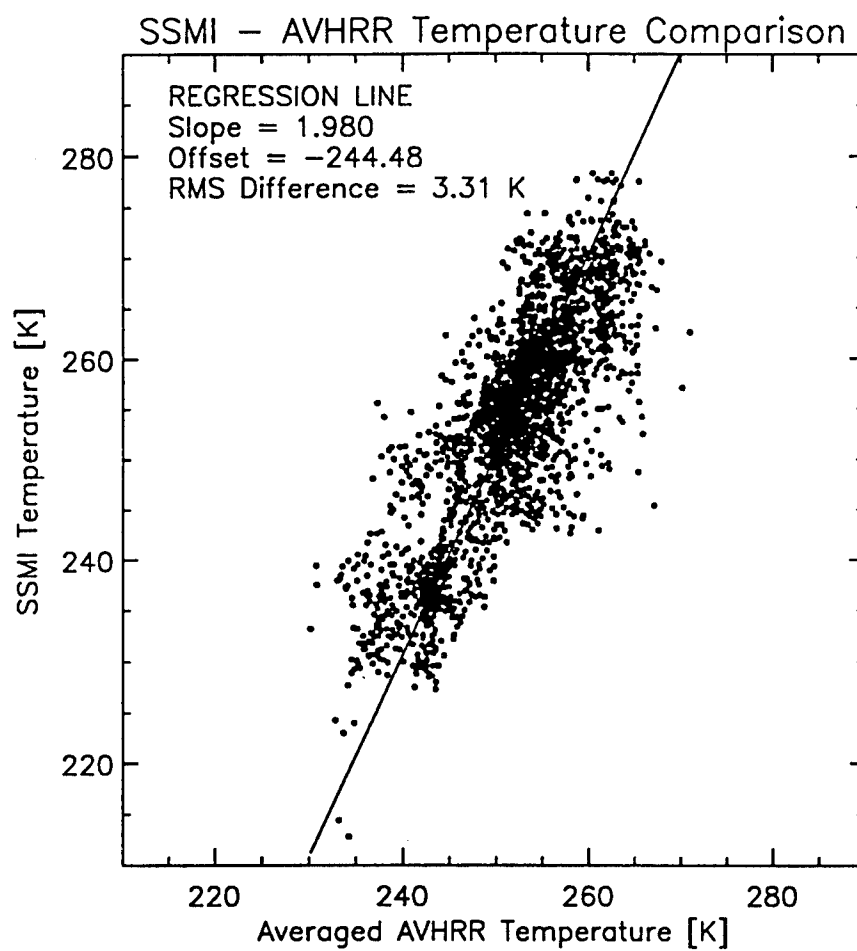


Figure 4.7. Cluster plot including all of the thirteen 512Km² study areas.

The scatter evident in Figure 4.7 may have several sources. Each of the remote sensing instruments is subject to random system noise that will propagate through the retrieval algorithm. This is addressed for the SSM/I temperatures in the next section. In addition, the spatial distribution of ice temperatures can change over the course of a day due to diurnal and weather effects, and also to movement of the ice pack, which can approach 50 Km/day [18]. At the low end of the cluster plot, the temperatures derived from the two sensors agree well, while at the upper end of the curve the SSM/I temperatures depart significantly from the AVHRR temperatures. At first glance, this difference appears to be a linear function of temperature itself. Closer examination reveals that the difference is instead related to the water concentration in each pixel, as shown in Figure 4.8. This explains why such a difference was not observed for the buoy comparisons. This comparison indicates that the SSM/I derived temperatures are currently susceptible to error in regions with large open water concentration, probably due to nonlinearities areas of frazil and thin new ice as suggested in Section 2.2.

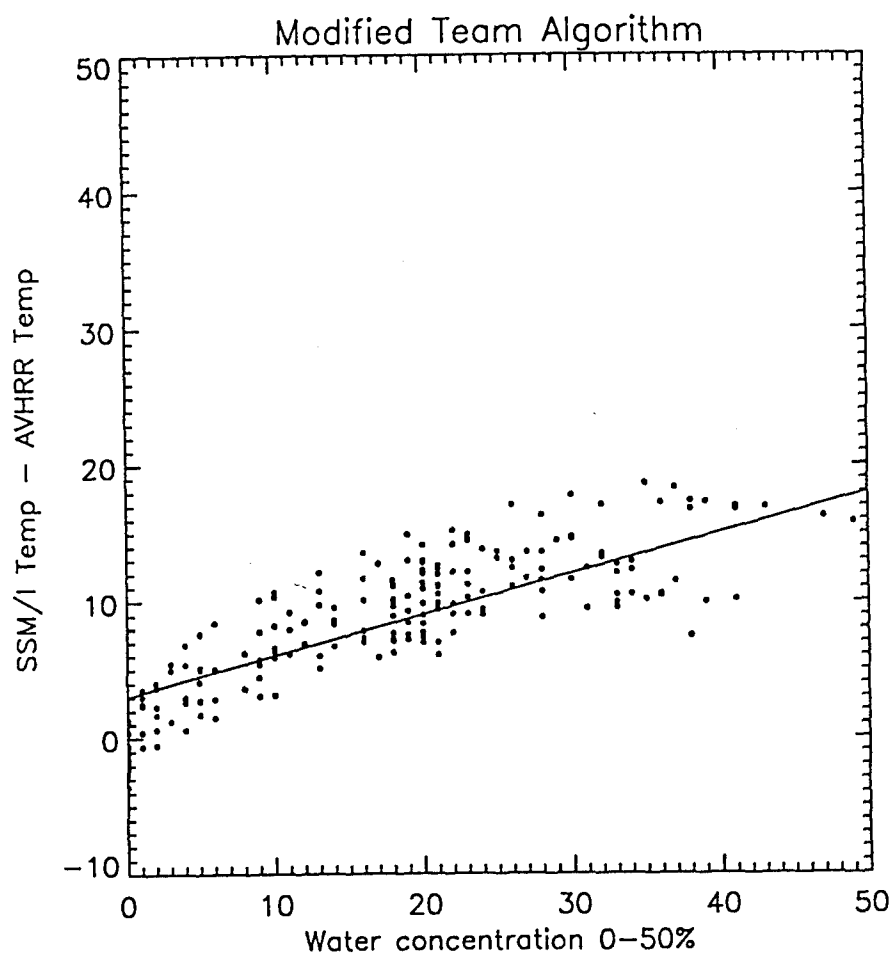


Figure 4.8. Difference between SSM/I derived temperatures and AVHRR derived temperatures plotted versus retrieved water concentration for the thirteen 512Km² study areas.

4.3 Weather Correcting Decision Algorithm

Increasing the accuracy of ice concentration and ice type information derived from microwave radiometry requires accounting for several second order effects, such as surface wind and atmospheric attenuation, which can contribute an uncertainty of several percent to the retrieved ice parameters. The superb calibration and extremely small ΔT of the Special Sensor Microwave/Imager (SSM/I) instrument give rise to the possibility of treating these effects as variables, thereby reducing the need for assumptions regarding local conditions. In principle, not only would ice concentration and type estimates be improved, but additional geophysical information, such as ice physical temperature and atmospheric vapor, would be available. An added advantage to this approach is that the second order parameters extracted, particularly the integrated atmospheric vapor and cloud liquid water, may help to interpret the 85 GHz brightness temperatures, which could then provide higher resolution images.

4.3.1 Algorithm Description

The Weather-Correcting Decision Algorithm was developed to utilize all of the low resolution SSM/I data. It therefore requires five input channels, the vertically polarized channels at 19, 22 and 37 GHz, and the horizontal channels at 19 and 37 GHz. The uniqueness of the algorithm lies in the routine that chooses the variables of primary concern for each pixel, making it possible to account for more variables than previously possible. The basis of the algorithm is the radiative transfer equation, which expresses the radiation received by the sensor as a function of the surface emissivity, the physical temperature of the surface, the atmospheric opacity, the

atmospheric upwelling and downwelling radiation, and the cosmic background noise. A detailed development of the atmospheric model was presented in Section 3.1.2, where the atmospheric attenuation and emission terms are expressed as functions of integrated atmospheric vapor (V) and integrated cloud liquid water (L) using high latitude climatological information. In addition, open water emissivity is modeled as a function of wind speed and the total surface emissivity is related, via a mixing formalism, to the emissivities of 'pure' surface types and relative concentrations.

The resulting radiative transfer equation yields a frequency dependent relationship between apparent brightness temperature (T_B) and a total of seven unknowns: first-year (C_{FY}), multi-year (C_{MY}), and water (C_W) concentrations, composite physical temperature (T_S), integrated atmospheric vapor (V), integrated cloud liquid water (L), and open water surface windspeed (W). Only six of these variables are independent, however, because the sum of C_{FY} , C_{MY} , and C_W must be unity. From Equations 3.7 and 3.32, the measured brightness temperature is:

$$T_{B,\lambda,p} = e_{\lambda,p} T_S e^{-\kappa_\lambda} + T_{B,\lambda,U_p} + (1 - e_{\lambda,p}) T_{B,\lambda,Down} e^{-\kappa_\lambda} + (1 - e_{\lambda,p}) T_{B,C} e^{-2\kappa_\lambda} \quad (4.6)$$

$$e_{\lambda,p} = F_{WAT} e_{WAT}(ws, \lambda, p) + F_{FY} e_{FY}(\lambda, p) + F_{MY} e_{MY}(\lambda, p) \quad (4.7)$$

The model for the increase in open water emissivity due to wind was developed by Goodberlet [19]. The wind-induced sea surface roughness, σ is:

$$\sigma = \sqrt{\frac{A_1 + A_2 * W}{1000}} \quad (4.8)$$

The variable, W represents the windspeed at a height of 20m above the surface, and the frequency dependent coefficients, A_1 and A_2 are given in Table 4.2

Table 4.2. Coefficients relating 20m windspeed to surface roughness, σ .

	Frequency		
	19 GHz	22 GHz	37 GHz
A_1	12.7	13.3	16.4
A_2	1.93	2.12	3.07

Table 4.3. Coefficients relating 20m windspeed to foam fraction, FF

	Frequency		
	19 GHz	22 GHz	37 GHz
B_1	-43.9	-54.4	-107.2
B_2	0.16	0.20	0.40
B_3	0.27	0.24	0.09

As discussed in Section 3.1.1, wind produces foam cover as well as roughness on the ocean surface. Foam effectively acts as a matching layer between air and water, which means the emissivity of foam covered areas is nearly one. The effective foam fraction of the pixel is expressed as:

$$FF = \frac{B_1 + B_2 T_s + A_3 W}{100}. \quad (4.9)$$

The coefficients for Equation 4.9 are frequency dependent and are presented in Table 4.3.

Given σ and FF and the coefficients in Table 4.4, the emissivity of the open water is calculated as follows:

$$e_{WAT}(ws\lambda, p) = FF + (1 - FF)(C_1 \sigma^2 + \frac{1000 C_2}{T_s} + C_3) \quad (4.10)$$

Table 4.4. Coefficients relating roughness, σ , and foam fraction, FF , to open water emissivity.

	Frequency & Polarization				
	19 GHz V	19 GHz H	22 GHz H	37 GHz V	37 GHz V
C_1	98.45	-199.48	102.85	122.68	-212.44
C_2	-70.00	-83.68	-76.11	-96.86	-107.70
C_3	362.3	501.0	380.1	436.0	571.0

At this point, all terms in Equation 4.6 have been defined in terms of the six geophysical variables for each frequency and polarization. Although each of the channels constitutes an independent measurement, the solution to Equation 4.6 remains underconstrained. At least one variable must be eliminated before the equation can be inverted. Since all six parameters are not expected to vary simultaneously, a routine was devised to decide which of the six variables are significant for a given scene.

Initially, all variables are set to a first guess value, and the algorithm begins in 'search mode': first order parameters (F_{FY} , F_{MY} , and T_s) are allowed to vary, while all others are held at constant, typical values. The Newton-Raphson minimum square error iterative technique is employed to arrive at a next guess for the varying parameters [20]. The algorithm then passes this information through a decision making routine, based primarily on the surface type fractions, to decide which of the higher order parameters will have significant effects. The routine is illustrated schematically in Figure 4.9, where descending levels represents successive iterations. For example, if the sum of the total ice concentration is greater than 0.5, it would be assumed that open water surface wind speed would have a negligible effect (Mode

4 at the third level in Figure 4.9). Furthermore, under these conditions, integrated cloud liquid water is not expected to be detectable. This leaves four variables for which to solve. In successive iterations, under certain conditions, integrated atmospheric vapor may also be eliminated as a variable. When the algorithm has completed its solution, a short routine converts the composite temperature to an ice temperature by assuming the open water fraction is at 272K.

Since this algorithm solves for parameters that may be rapidly changing, it requires swath data as input instead of averaged, gridded data. By linearly averaging non-linear data second order information is lost and in fact, looks like noise. This problem has been discussed by Rothrock and Thomas [21] with regard to SMMR brightness temperatures.

4.3.2 Algorithm Product Evaluation

The retrieved ice fractions compare favorably with those of previously validated algorithms. Data comparisons at several locations indicate a difference of seven to ten percent in total ice concentration, and significantly more multiyear ice in areas of 100% ice concentration. The increased multiyear ice retrieval is encouraging because there is strong evidence that the NASA Team algorithm underestimates multiyear ice concentration even in the winter months [22].

Images of the integrated atmospheric vapor retrieval show that areas of increased vapor are coincident with areas of known storm activity or high lead density. One example is presented in Figures 4.10, 4.11, 4.12. Figure 4.10 is an image of atmospheric water vapor retrieval, where the lighter area in the Beaufort Sea indicates increased atmospheric vapor. The AVHRR visible frequency image in Figure 4.11 indicates that a roughly rectangular cloud is present in the Beaufort Sea in addition

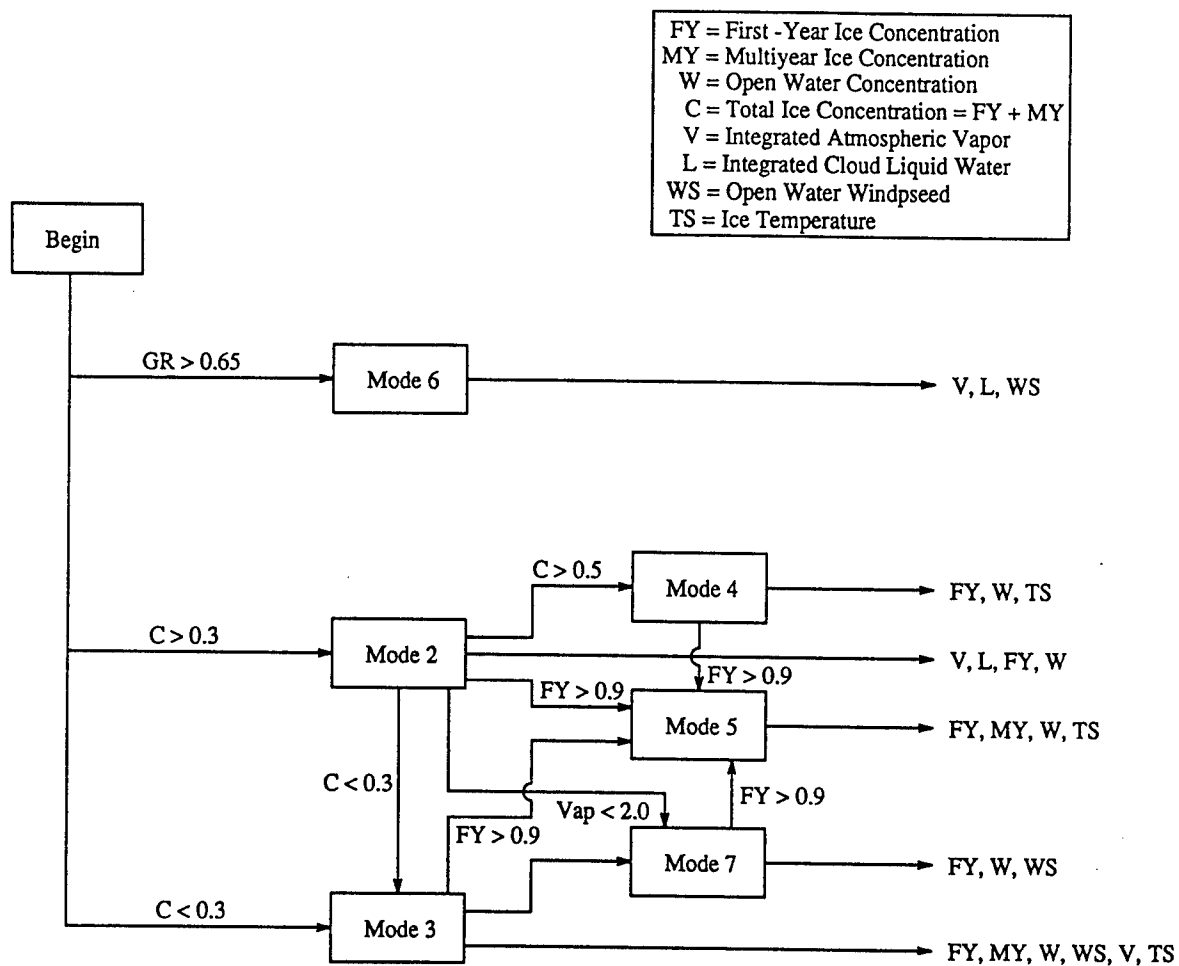
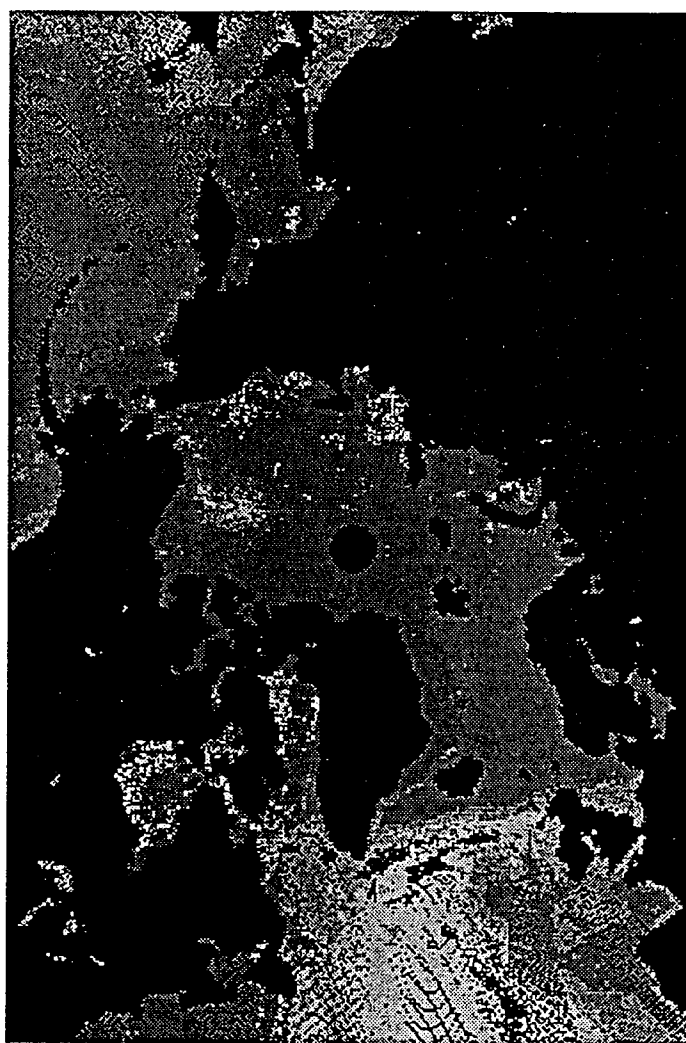


Figure 4.9. Schematic representation of the Decision routine that decides which of the six possible variables, (C_{FY} , C_{MY} , W , T_S , V , L), should be of primary concern for a given pixel.

to a large cloud mass in the Bering Strait. Comparing this with the infrared image in Figure 4.12, the cloud mass in the Beaufort appears to be nearly as warm as the open ocean. This indicates that the Beaufort Sea cloud is at the atmospheric temperature inversion layer, and therefore contains significant water vapor.

Ice temperature retrieval images have been compared with climatological contour maps that indicated that regional temperature variations are well represented, as indicated in Figure 4.13 and 4.14. As in Section 4.2, the calculated temperatures were also compared with buoy measurements from the Polar Science Center (University of Washington). In spite of the inherent differences between the two measurements, the correlation coefficient was 0.78 in March, as shown in Figure 4.15. Figure 4.16 shows a time series comparison of buoy temperatures and temperature produced by both the modified NASA Algorithm and the Decision Algorithm.

The temperatures were also compared with the March 11, 1989 AVHRR image introduced in Figure 4.3. The results of the comparison were very similar to those obtained with the Modified Team Algorithm. That is to say, the correlation coefficient was relatively high, but the slope was much greater than one. Figure 4.17 shows the relationship between the temperature residual ($\text{SSM/I Temp} - \text{AVHRR Temp}$) and the retrieved water concentration. The correlation coefficient for these data is 0.928, and the slope of the regression line is 0.83 with an offset of 0.59. As was the case for the Modified Team Algorithm, the slope evident in Figure 4.17 indicates that either the open water emissivity is not accurate, or that all geophysical variables (such as frazil and thin ice) are not included in the model.



Atmospheric Vapor [Kg/m^2]



Figure 4.10. Integrated Atmospheric Water Vapor derived from the Decision Algorithm for March 11, 1988

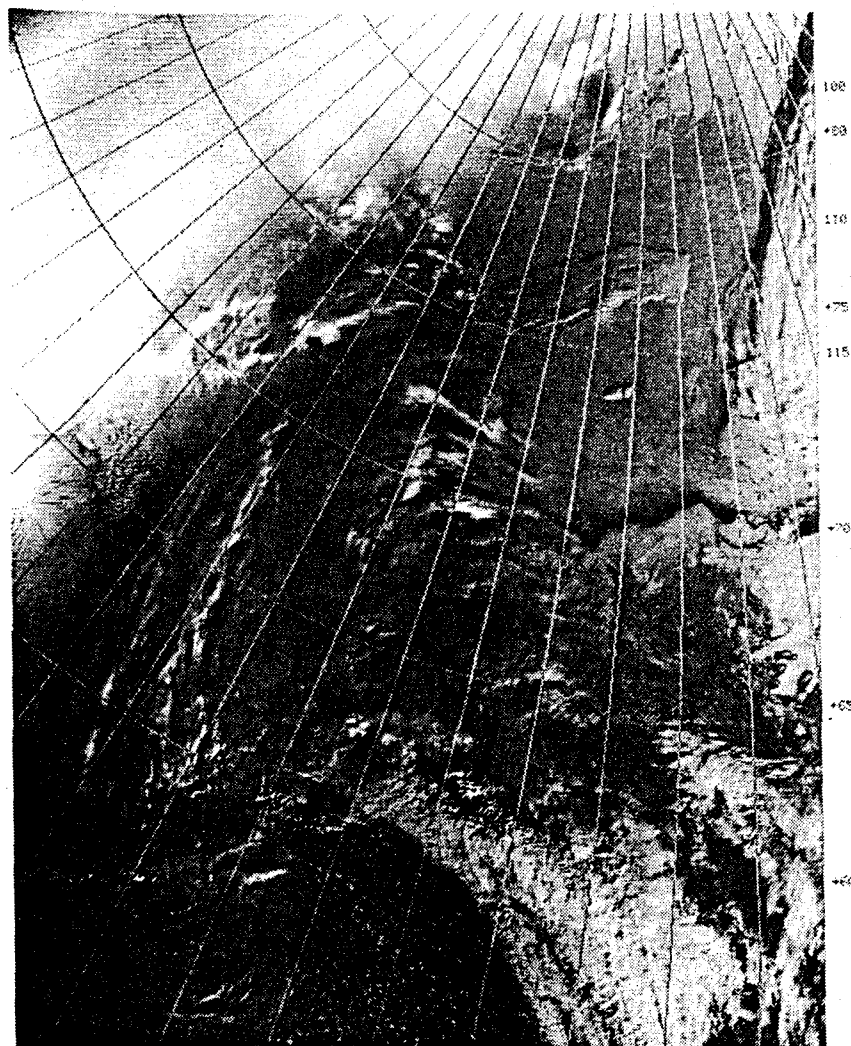


Figure 4.11. Visible frequency image from AVHRR. The region of interest is the white rectangular cloud in the Beaufort Sea.

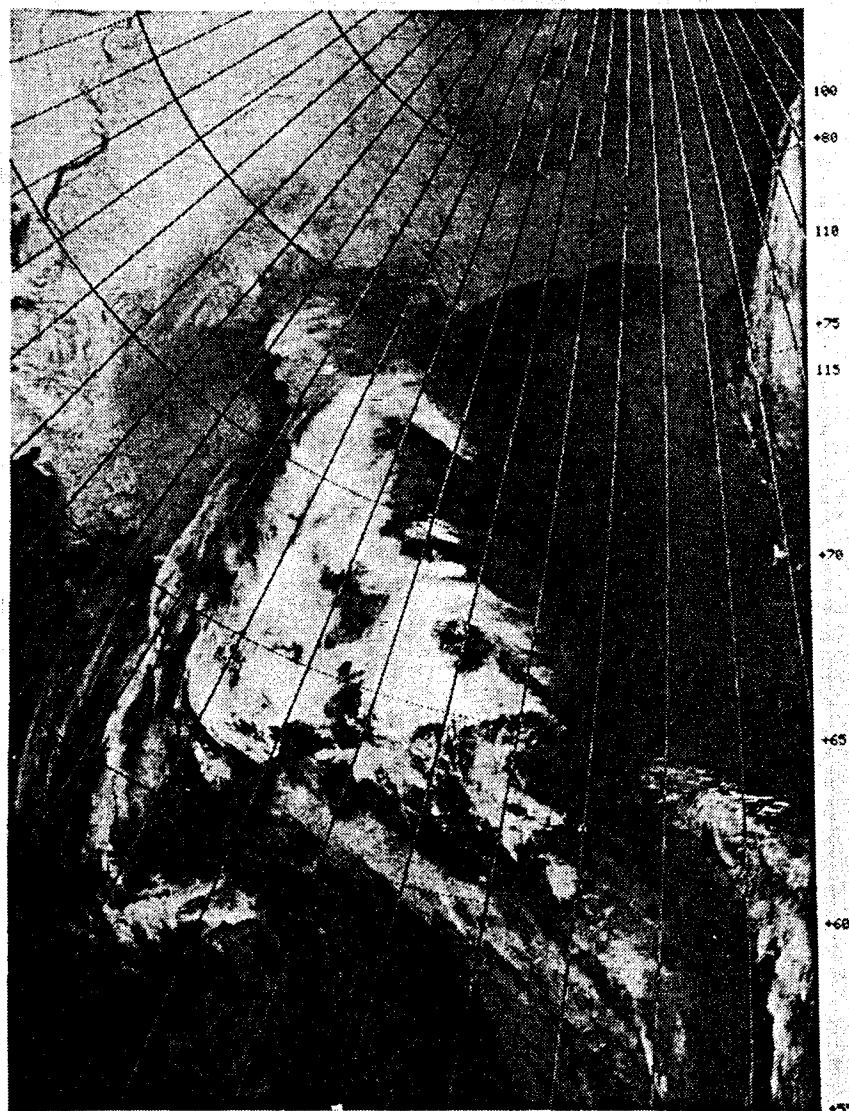


Figure 4.12. Infrared image from AVHRR. The area of interest appears as a dark (warm) rectangle in the Beaufort Sea.



Figure 4.13. Image of ice temperature retrieval for March 11, 1988. Land has been masked in black.

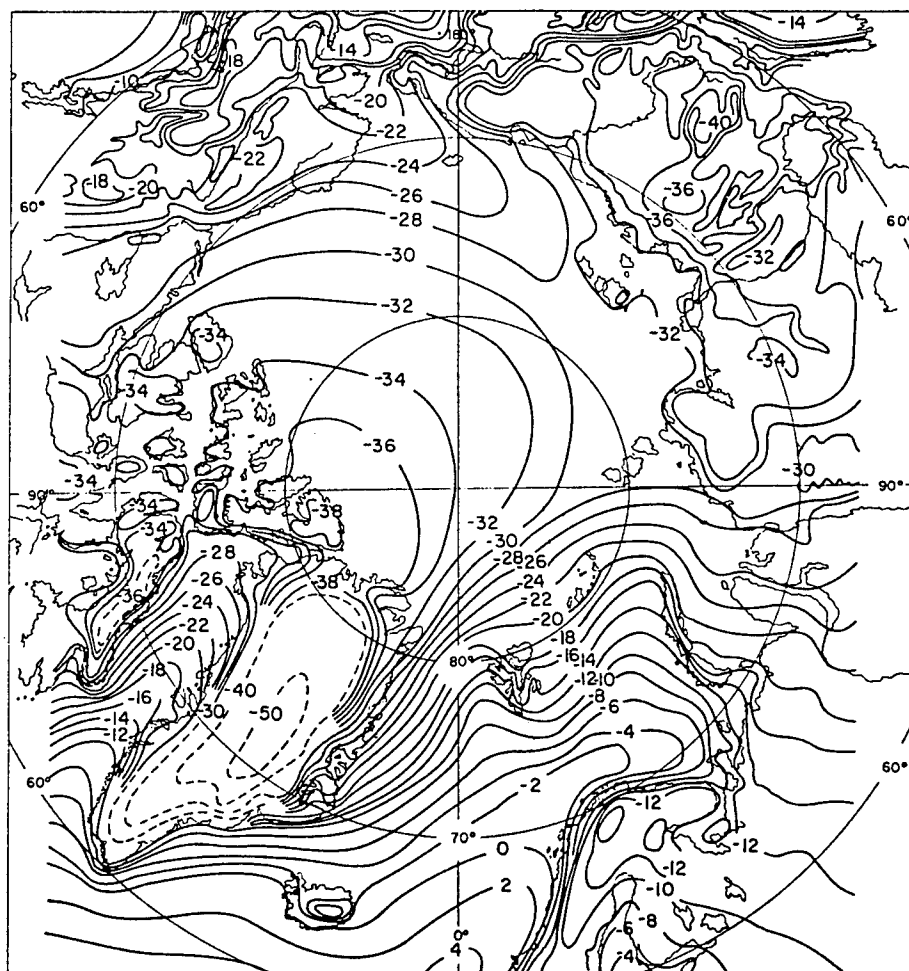


Figure 4.14. Average temperature contours for March [4].

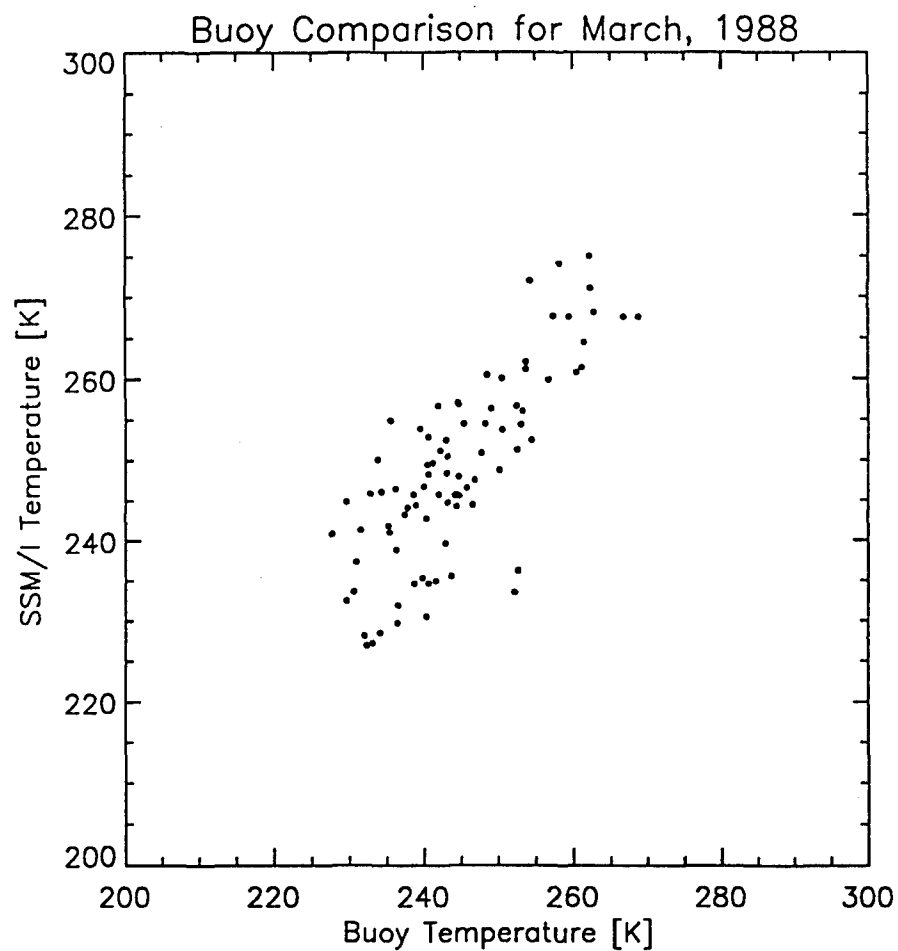


Figure 4.15. Scatter plot of ice temperature as retrieved by the Decision Algorithm vs. air temperature measured by AOBP Buoys in March, 1988. The slope of the regression line is 0.78, the correlation coefficient is 0.78 and the rms difference is 4.9K

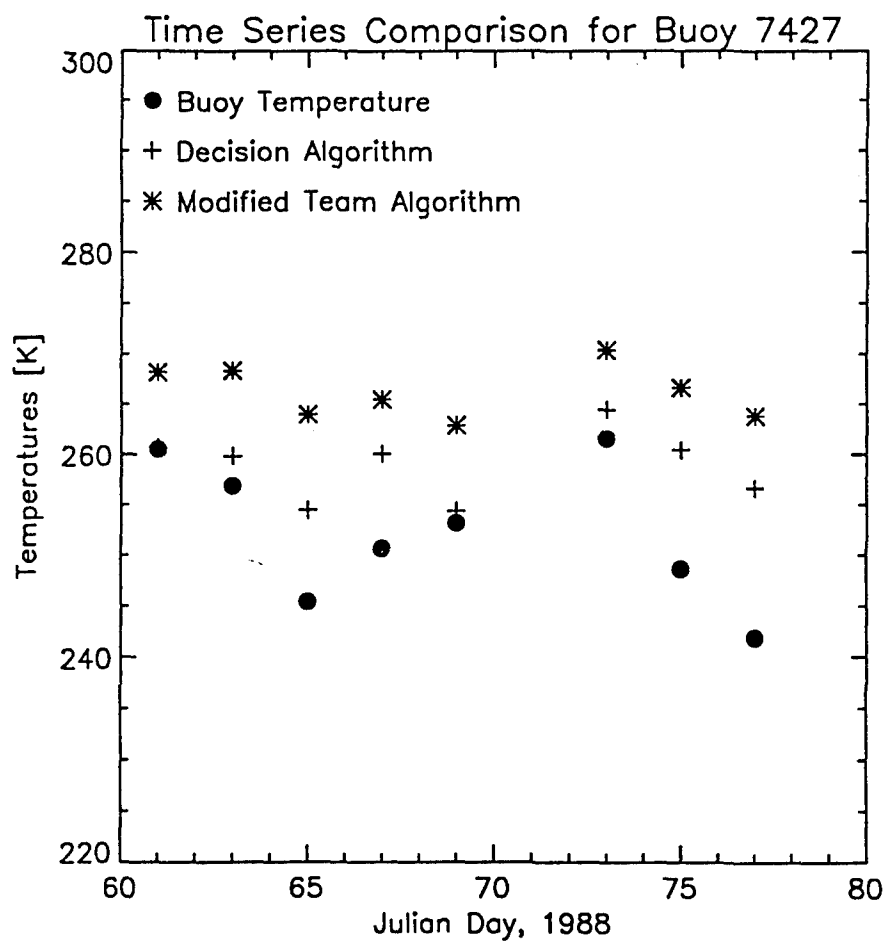


Figure 4.16. Time series comparison for every odd day in March, 1988

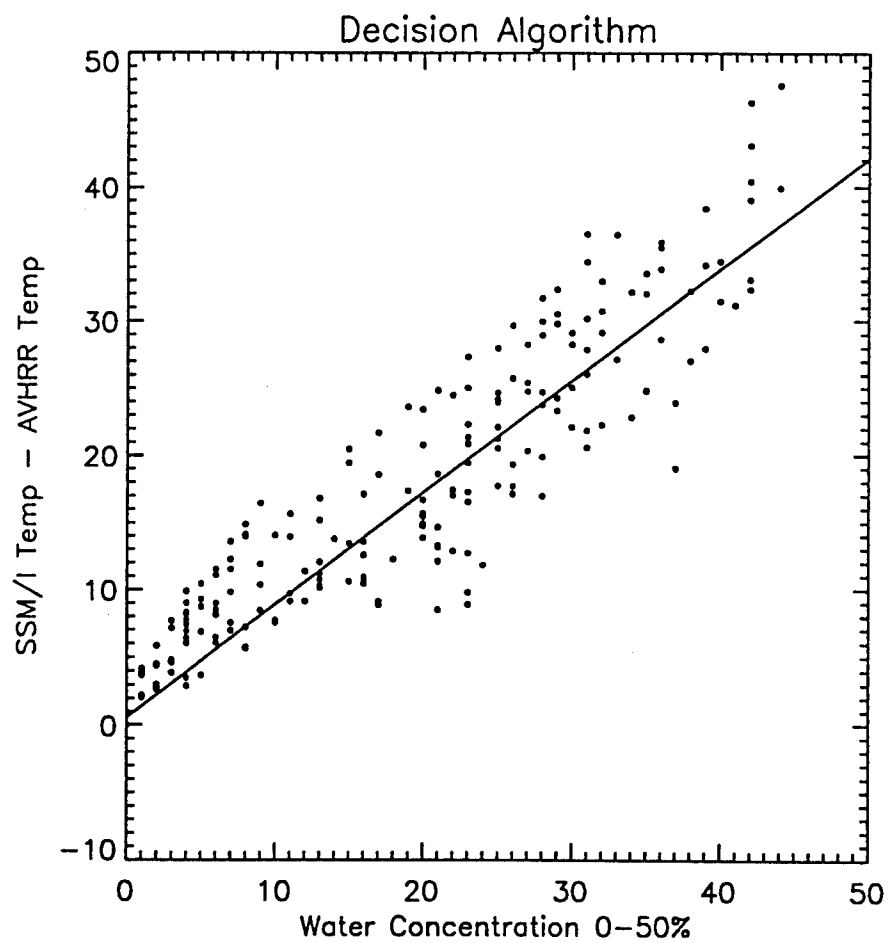


Figure 4.17. Difference between SSM/I derived temperature and AVHRR derived temperature plotted versus retrieved water concentration (0 - 50%)

4.3.3 Sensitivity Analysis

A sensitivity analysis investigated the stability and precision of the algorithm when noise is present on the brightness temperature signal. To isolate the noise effect, the analysis used simulated brightness temperature data generated for a typical range of surface and atmosphere conditions. White Gaussian noise was added to each set of temperatures and the algorithm was run on the noisy data. The variance of the added noise was determined in two different ways: the first defined the standard deviation as 1K, allowing for easy comparison with other algorithms regardless of sensor; the second used a standard deviation equal to those previously reported for each of the SSM/I channels [12], which appear in Table 4.5. The standard deviation of the products retrieved from the noisy simulated brightness temperatures as compared to the products retrieved from the clean brightness temperatures is presented in Table 4.6 for each of the noise levels.

Table 4.6 indicates that the ice concentration and type are extremely insensitive to instrument noise on the order of that observed for the SSM/I. Even when noise with a standard deviation of 1K is introduced, the error in total ice concentration is only 5%. The integrated atmospheric vapor is the parameter which is most sensitive to noise. This is because the calculation of vapor depends heavily on the 22V channel, which is the noisiest channel. The effect of instrument noise on the temperature measurement arises because, to first order, the physical temperature is the brightness temperature divided by the emissivity. Since the emissivity of any surface type is less than unity, any noise in brightness temperature will be amplified. Clearly this effect is minimal over areas of 100% first year ice (high emissivity), slightly greater over areas of 100% multiyear ice, and a maximum

over areas containing a large percentage of open water. Therefore, under normal winter conditions, the standard deviation associated with the surface temperature in Table 4.6 is expected to be a worst case estimate.

To further estimate confidence levels in the output products, their sensitivity to model errors was investigated. The two parameters expected to contribute the largest errors to the primary products (total ice concentration and multiyear ice concentration) are the emissivity of multiyear ice, and the emissivity of first-year ice when thin ice is present. These effects were examined using simulated brightness temperature data over a broad range of surface types.

Random white Gaussian noise was added to the emissivity of multiyear ice as the test brightness temperatures were generated. The following two cases were examined: 1) The added signal was zero mean white noise with standard deviation of 0.01 (1%), and 2) the added signal was zero mean white noise with standard deviation of 0.005 (0.5%). The standard deviations of the output products, as compared with the known starting values for these products, are given in Table 4.7 for each of the noise levels.

Table 4.7 suggests that the error in total ice concentration due to variable multiyear ice signal is on the order of 1% over a 0.02 change in emissivity. The error in the multiyear ice concentration is larger, at just under 3% over the same range. The noise on the temperature retrieval was less than 2K as compared with the original input temperature, showing some sensitivity. The vapor retrieval shows the greatest sensitivity to uncertainty in emissivity. This is again because the vapor retrieval depends heavily on one channel, while the other parameters depend more or less evenly on all channels. When noise is introduced independently on all channels, its

Table 4.5. Typical standard deviation of instrument noise for each SSM/I channel in Kelvins.

Frequency and Polarization				
19 GHz V	19 GHz H	22 GHz V	37 GHz V	37 GHz H
0.45	0.42	0.75	0.37	0.39

Table 4.6. Standard deviation of algorithm products as a result of noise introduced on the brightness temperature data.

	Total Ice Conc.	Multiyear Ice Conc.	Int. Atm. Vapor	Int. Atm. Liquid	Surface Temperature
SSM/I Noise	0.0065	0.0099	1.34	0.011	0.998
1 K Noise	0.0504	0.024	2.38	0.003	2.30

Table 4.7. Standard deviation of algorithm products as a result emissivity errors.

	Total Ice Conc.	Multiyear Ice Conc.	Int. Atm. Vapor	Int. Atm. Liquid	Surface Temperature
0.005 Noise	0.0060	0.0127	1.13	0.010	0.864
0.01 Noise	0.0120	0.0253	2.26	0.002	1.74

effect is minimized for parameters that show no frequency preference, while the a frequency specific parameter suffers errors proportional to the introduced noise.

Finally, the effect of thin ice within the footprint was examined. Thin ice has an emissivity between that of water and that of thick first year ice (which depends on thickness and frequency). Since the algorithm does not allow for variable emissivity, such a signature would be interpreted as a combination of open water and first year ice. The retrieved products behaved predictably when simulated data were processed. For example, when the pixel was comprised of 50% water, 40% first-year ice, and 10% thin ice, the output of the algorithm varied between 60% water and 40% first year ice, and 50%water and 50% first year ice, depending on the chosen emissivity of the thin ice area. This analysis assumed that the linear increments in the emissivity occurred evenly across the spectrum. Although this is not strictly true in nature, it serves as a reasonable indicator of algorithm behavior. The degree to which this is not true would determine a preference toward overestimating first year ice concentration.

Since the two types of errors mentioned above are independent, their effects would be additive. This indicates that an estimate of the uncertainty in total ice concentration estimate is less than 1%, while 5% is a conservative estimate for RMS uncertainty in the multi-year ice concentration.

4.3.4 Implications for an 85 GHz high resolution mode

The motivation behind the development of the Decision Algorithm was to provide atmospheric correction for the 85 GHz vertical and horizontal SSM/I channels. Because the attenuation coefficient for cloud liquid water increases as the square of frequency, the 85 GHz channels are especially susceptible to atmospheric contam-

ination, even in the relatively dry polar regions. Correction for these channels is desirable, however, because the SSM/I antenna provides 12.5 km ground resolution at 85 GHz, which would significantly enhance the ice edge.

Figure 4.18 is an image of 85 GHz horizontally polarized data for the 25th of April, 1988. This date was selected because the polar grid contained areas of both fair weather clouds and more severe storm clouds. It is very difficult to distinguish a clear ice edge in this image, even in the Norwegian and Barents Seas, which contain only light cloud cover.

In Figure 4.19 the 85 GHz horizontal brightness temperatures have been corrected using the output from the decision algorithm. The atmospheric parameters are assumed constant over each 25 Km resolution cell in the product grids. For each 12.5 Km 85 GHz resolution cell, the surface temperature, atmospheric vapor, and cloud liquid estimates are taken from the corresponding low resolution cell. The relationships for T_A , κ_{VAP} , κ_{LIQ} , and κ_{O_2} at 85 GHz were derived in the manner presented in Section 3.1.2.

$$\kappa = \kappa_{VAP} + \kappa_{LIQ} + \kappa_{O_2} \quad (4.11)$$

$$\kappa_{VAP} = V \left(\frac{e^{0.836(T_s - 203.6)}}{1000.} \right) \quad (4.12)$$

$$\kappa_{LIQ} = L \left(2512e^{-6.866(1+0.0045(T_s-273.15))} \right) \quad (4.13)$$

$$\kappa_{O_2} = \frac{52.25 - 0.1566T_s}{100.} \quad (4.14)$$



Figure 4.18. Arctic brightness temperatures at 85 GHz horizontal polarization.

The radiative transfer equation for the atmosphere is then solved for the (atmosphere corrected) surface brightness temperature as follows:

$$T_{Bcor} = T_s \frac{T_B - T_A(1 - e^{-\kappa})(1 + e^{-\kappa}) - T_c e^{-2\kappa}}{T_s e^{-\kappa} - T_A(1 - e^{-\kappa})e^{-\kappa} - T_c e^{-2\kappa}} \quad (4.15)$$

The ice edge is effectively enhanced in Figure 4.19, particularly in the Barents and Greenland Seas and Baffin Bay. The large area in the Denmark Strait and North Atlantic (south and west of Iceland) which remains ambiguous is due to a strong weather front which could not be resolved by the weather correction algorithm. Such atmospheric conditions saturate even the lower frequency channels, and may only be eliminated by thresholding or clipping. Thus, the weather correction is very effective for normal weather conditions but is not as reliable in areas of heavy storm activity. Figure 4.20 is an expanded view of the total retrieved ice concentration derived from the decision algorithm at the ice edge in the Greenland Sea. Figures 4.21 represents the raw brightness temperatures at 85 GHz horizontal polarization over the same area, and Figure 4.22 shows the atmosphere corrected 85 GHz brightness temperatures. Again the contrast between open water and ice is enhanced, and as expected, the image resolution is improves.

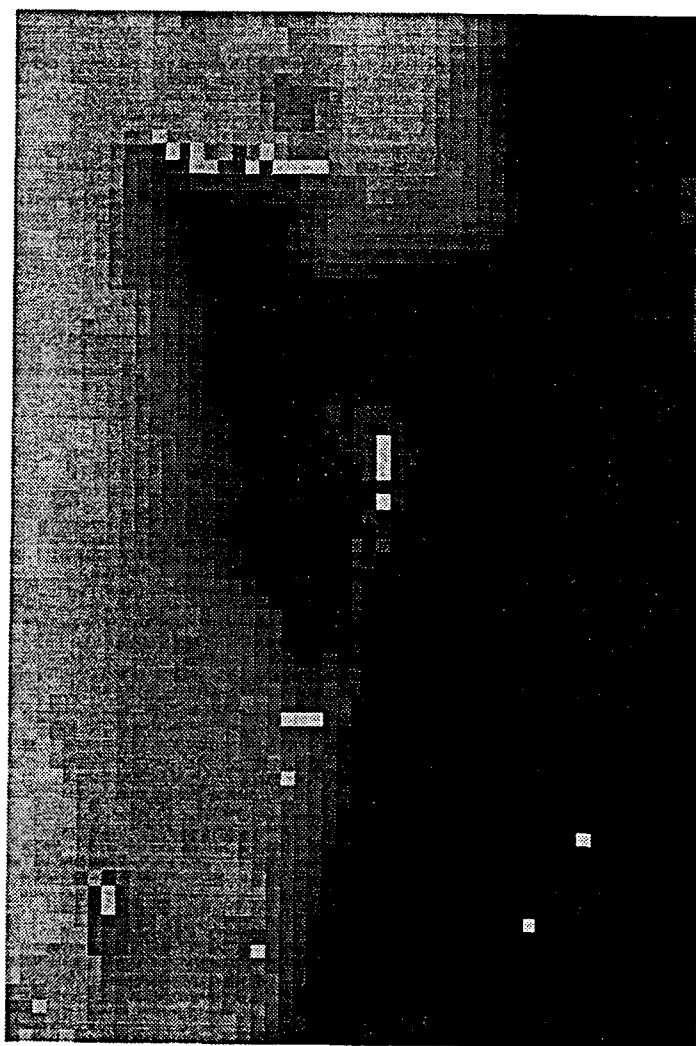
The variability in brightness temperature apparent in the open water areas in Figures 4.19 and 4.22 is due in part to varying sea surface wind conditions and in part to the fact that the 85 GHz channel is more sensitive to variation in cloud liquid than the 37 GHz channels used for the correction. Thus, small random errors in the liquid estimate caused by system noise on the lower channels are amplified in the correction of the higher frequency channels. The only way to eliminate the propagation of such errors is to expand the decision algorithm to include the 85



140 K

270 K

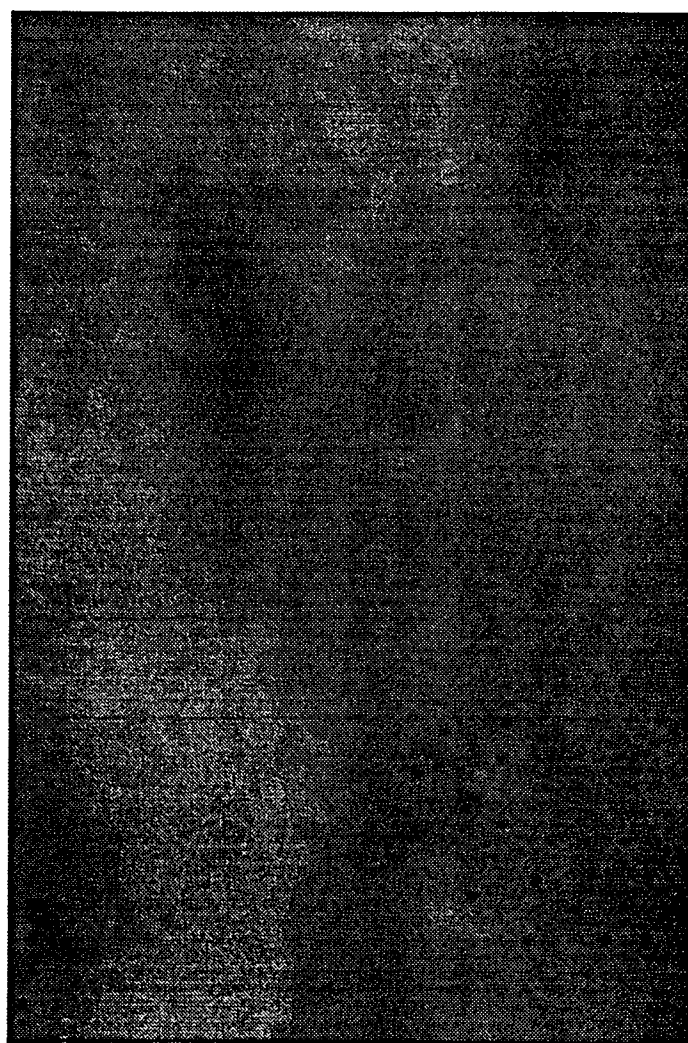
Figure 4.19. Arctic brightness temperatures at 85 GHz horizontal polarization corrected for atmospheric vapor and cloud liquid water.



140 K

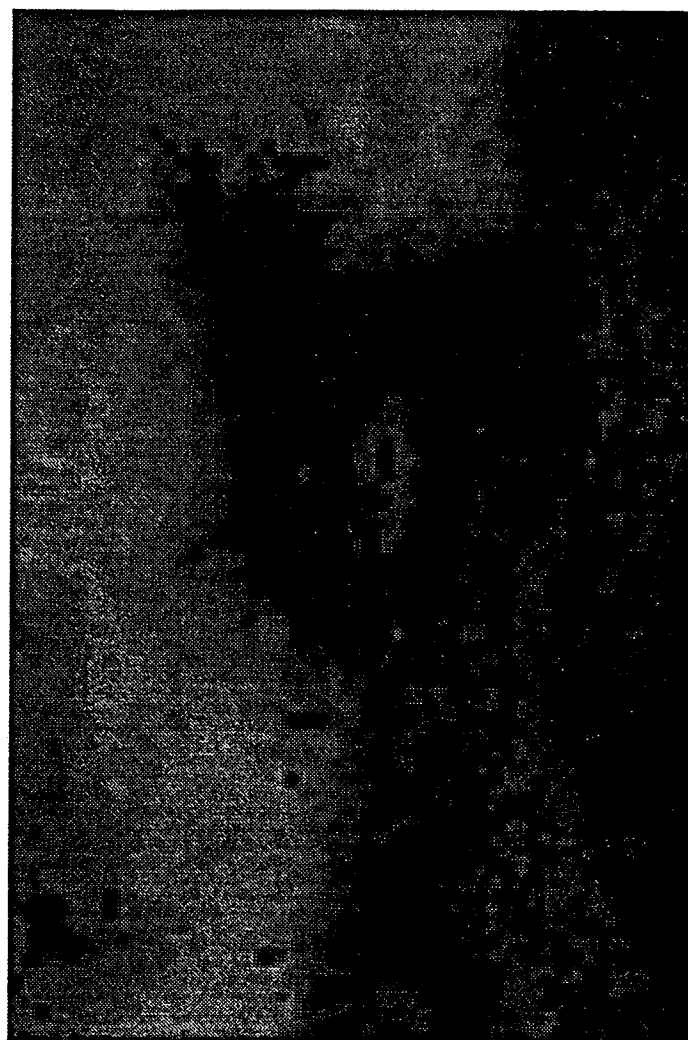
270 K

Figure 4.20. Total ice concentration as derived from the decision algorithm for the Greenland Sea on April 25, 1988



140 K 270 K

Figure 4.21. Brightness Temperature at 85 GHz horizontal polarization in the Greenland Sea on April 25, 1988



140 K

270 K

Figure 4.22. Surface brightness temperature at 85 GHz horizontal polarization. The atmospheric attenuation was calculated from the integrated cloud liquid water and atmospheric vapor estimates from the decision algorithm.

GHz channels, with their resolution degraded, and then follow the same procedure to correct the high resolution 85 GHz data with the resulting vapor and cloud liquid estimates.

CHAPTER 5

CONCLUSION

The polar regions play a crucial role in global climatology, biology, and commercial trade. The harsh environment in these regions make long term synoptic monitoring of surface and atmospheric conditions difficult. Airborne and satellite observation platforms are therefore the logical alternatives to in situ observation. Microwave radiometry is particularly well suited to polar remote sensing because microwaves suffer little attenuation under the usual polar atmospheric conditions (fog, cloud cover, and 'diamond dust').

Microwave radiometers aboard satellite platforms in polar orbit have been operational for over two decades. To date, the data analysis has focused on the first order variables of ice concentration and type, primarily due to instrument limitations. These algorithms have surpassed all performance expectation, but with the launch of the SSM/I in 1987, a new era in polar microwave radiometry became possible. Additional geophysical information is needed in the push toward a more thorough understanding of the role of polar sea ice in the global climate system. The well calibrated multi-channel SSM/I system provides an opportunity to estimate first order parameters more accurately and to estimate several additional second order effects. The following paragraphs summarized what I believe to be the major contributions of this dissertation to the larger effort of polar remote sensing.

Much of the heat lost from the ocean to the atmosphere in the arctic winter occurs through new and refrozen leads and polynas. Estimates of ice thickness in

such areas would significantly enhance the accuracy of heat budget calculations. The difficulty is that, in the early stages of growth, the dielectric constant changes rapidly, along with the ice thickness. This dissertation contributes to the ongoing effort by developing a method to measure the dielectric constant, or permittivity, remotely. To our knowledge, this is the first attempt at such a task. The approach presented could be easily modified to estimate thickness as well as dielectric constant using spectral information. The limitation of this approach is its reliance upon the smooth boundary model, where "smoothness" is defined relative to wavelength. Furthermore, the entire footprint is assumed homogeneous, which, with current technology, nearly eliminates the possibility of applying the technique from satellite on all but large polynas.

Physical surface temperature is another geophysical variable which is necessary in climatological studies. Currently, global climate models rely on data from drifting buoys for ice pack surface temperature measurements. These buoys are sparsely located and often unreliable. A technique to estimate ice temperature from SSM/I data, the modification to the Team Algorithm, was developed in this dissertation. The temperature estimates compared favorable with estimates derived from thermal infrared data. The major advantage of the microwave derived temperatures over the infrared derived temperatures is, again, that infrared measurements are susceptible to atmospheric contamination, even after appropriate cloud masking, while moderate atmospheric effects can be accounted for at microwave frequencies. Although the correlation between the two data sets was good, the slope of the SSM/I versus clear sky AVHRR Temperatures plot is still bothersome. It appears to be related to open water concentration, which may indicate a problem with the open water tie

point or, more likely, a non-linearity introduced by the presence of thin ice.

The third major contribution of this work lies in the area of atmospheric correction. The weather correcting Decision Algorithm employs the powerful combination of the Newton-Raphson technique and Minimum Squared Error solutions to estimate the atmospheric variables in the radiative transfer equation. To our knowledge, this is the first time such an attempt has been made for the well calibrated SSM/I data over the Arctic. Although very little atmospheric "truth" is available, the increased atmospheric vapor estimates in areas of increased lead distribution or storm activity provide qualitative support for the technique. These estimates of atmospheric vapor contribute in two ways to the study of the polar regions. First, since most of the atmospheric vapor over the ice pack is derived from open water leads, the vapor estimates may provide information about lead density and type (open vs. refrozen), which in turn may be used in heat budget calculations. The second and perhaps more important implication of the ability to estimate atmospheric parameters is the possibility to apply the retrieved vapor and liquid values to enhance the high resolution 85 GHz channels. To date these two channels have remained unused because atmospheric contamination made ice indistinguishable from water. When the atmospheric parameters are subtracted from the 85 GHz data, a much cleaner, 15 km resolution image is obtained. Successfully correcting for the atmosphere doubles the resolution of the passive microwave imagery available, which is of particular importance in lead, polyna, and ice edge studies.

This dissertation seeks to contribute to the studies of global systems, from scientific to commercial, by providing a geophysical picture of a region that only a lucky few have ever seen. It is my hope that this work also contributes to global efforts to understand and protect our complex and intriguing environment.

APPENDIX: SFMR WINDSPEED ALGORITHM

Equation 3.31 in Section 3.1.1 must be solved for γ , which is related only to ocean surface windspeed. This is accomplished in the following manner. First, Equation 3.31 is simplified to:

$$t_i = a_i + \gamma b_i \quad (\text{A.1})$$

where the subscript i denotes frequency. If t_i , a_i and b_i are known, γ must be chosen to minimize the difference between theoretical and measured brightness temperatures. Using inner product notation:

$$\sum_{i=1}^n (t_i - a_i - \gamma b_i)^2 = (T - A - \gamma B, T - A - \gamma B) \quad (\text{A.2})$$

$$= (T - A, T - A) - 2(T - A, \gamma B) + (\gamma B, \gamma B) \quad (\text{A.3})$$

Setting the derivative with respect to γ equal to zero and dividing yields :

$$\gamma = \frac{(T - A, B)}{(B, B)} \quad (\text{A.4})$$

This solution for γ is directly mapped to windspeed. The second unknown in Equation 3.31 is rainrate, R , which is non-linearly related to κ_{R_i} and κ_{r_i} in Equation 3.31 by:

$$\kappa_{R_i} = e^{-g f_i^n R^b H} \quad (\text{A.5})$$

$$\kappa_{r_i} = e^{-gf_i^n R^b h} \quad (\text{A.6})$$

where h is the aircraft altitude, H is the mean height of the precipitation column (typically 2 Km), R is the rainrate in *mm/hour*, and g , b , and n are empirically derived:

$$n = 2.6R^{0.0736}$$

$$g = 1.87 \times 10^{-9} \left[\frac{\text{nepers}}{\text{meter}} \right]$$

$$b = 1.35$$

(A.7)

Solving for a minimum in Equation A.2 results in transcendental equations, so an iterative approach is used. The derivative of Equation 3.31 with respect to R is:

$$\frac{\delta}{\delta R} (T - A - \gamma B, T - A - \gamma B) = \frac{\delta}{\delta R} [(T, T) - 2(T, A + \gamma B) \quad (\text{A.8})$$

$$+ 2(A + \gamma B, A + \gamma B)]$$

$$= -2 \left(T, \frac{\delta}{\delta R} (A + \gamma B) \right) \quad (\text{A.9})$$

$$+ 2 \left(A + \gamma B, \frac{\delta}{\delta R} (A + \gamma B) \right)$$

which implies:

$$\left(A + \gamma B - T, \frac{\delta}{\delta R} A + B \frac{\delta \gamma}{\delta R} + \gamma \frac{\delta B}{\delta R} \right) = 0 \quad (\text{A.10})$$

at a minimum:

$$\frac{\delta \gamma}{\delta R} = \frac{\delta}{\delta R} \frac{(T - A, B)}{(B, B)} \quad (\text{A.11})$$

$$= \frac{\left(T - A, \frac{\delta B}{\delta R} \right) - \left(\frac{\delta A}{\delta R}, B \right)}{(B, B)} \quad (\text{A.12})$$

$$= \frac{2(T - A, B) \left(B, \frac{\delta B}{\delta R} \right)}{(B, B)^2} \quad (\text{A.13})$$

From Equations 3.31 and A.1 :

$$\frac{\delta a_i}{\delta R} = \frac{\delta \kappa_{r_i}}{\delta R} \kappa_{a_i} [(1 - \mu_i) \kappa_{R_i} \rho_i + T_R - T_A - \mu_i (T_R - T_S)] \quad (\text{A.14})$$

$$+ \kappa_{r_i} \kappa_{a_i} \frac{\delta \kappa_{R_i}}{\delta R} (1 - \mu_i) \rho_i$$

$$\frac{\delta b_i}{\delta R} = \alpha_i \frac{\delta \kappa_{r_i}}{\delta R} \kappa_{a_i} [T_S - T_R - \kappa_{R_i} \rho_i] - \alpha_i \kappa_{r_i} \kappa_{a_i} \frac{\delta \kappa_{R_i}}{\delta R} \rho_i \quad (\text{A.15})$$

From Equations A.5 and A.6:

$$\kappa_{R_i} = e^{-gH \exp[b \ln R + l_i R^p]} \quad (\text{A.16})$$

$$\frac{\delta \kappa_{R_i}}{\delta R} = -gH \left(\frac{b}{R} + l_i \rho R^{p-1} \right) e^{(b \ln R + l_i R^p)} e^{-gH \exp(b \ln R + l_i R^p)} \quad (\text{A.17})$$

$$\frac{\delta \kappa_{r_i}}{\delta R} = -gh \left(\frac{b}{R} + l_i \rho R^{p-1} \right) e^{(b \ln R + l_i R^p)} e^{[-gh \exp(b \ln R + l_i R^p)]} \quad (\text{A.18})$$

Therefore, to solve Equation A.10, thus finding a minimum for Equation A.2, substitute Equations A.16, A.17, A.18, and A.5 into Equations A.14, A.15, and 3.31 to obtain the vectors needed for Equation A.10. If the equality in A.10 is not satisfied, R is adjusted according to the flow chart in figure A.1, and the procedure is repeated.

The atmospheric opacity, τ_A , is generated for a standard tropical atmosphere. For each of the frequencies of the SFMR, the value of κ_A is given in Table A.1.

Table A.1. Atmospheric opacity for each of the SFMR frequencies

Frequency	4.63	5.915	6.771	7.20	6.344	5.056
κ_A	0.9897	0.9885	0.9875	0.9870	0.988	0.9893

The fractional atmospheric transmissivity below the aircraft at altitude h is:

$$\kappa_{a_i} = \kappa_{A_i}^{(1 - \exp(h/3500.))} \quad (\text{A.19})$$

The air temperature at 4500 meters altitude in terms of measured aircraft ambient temperature is calculated using the following lapse rate:

$$T_A = T_{\text{aircraft}} - 0.0058 (4500 - h) \quad (\text{A.20})$$

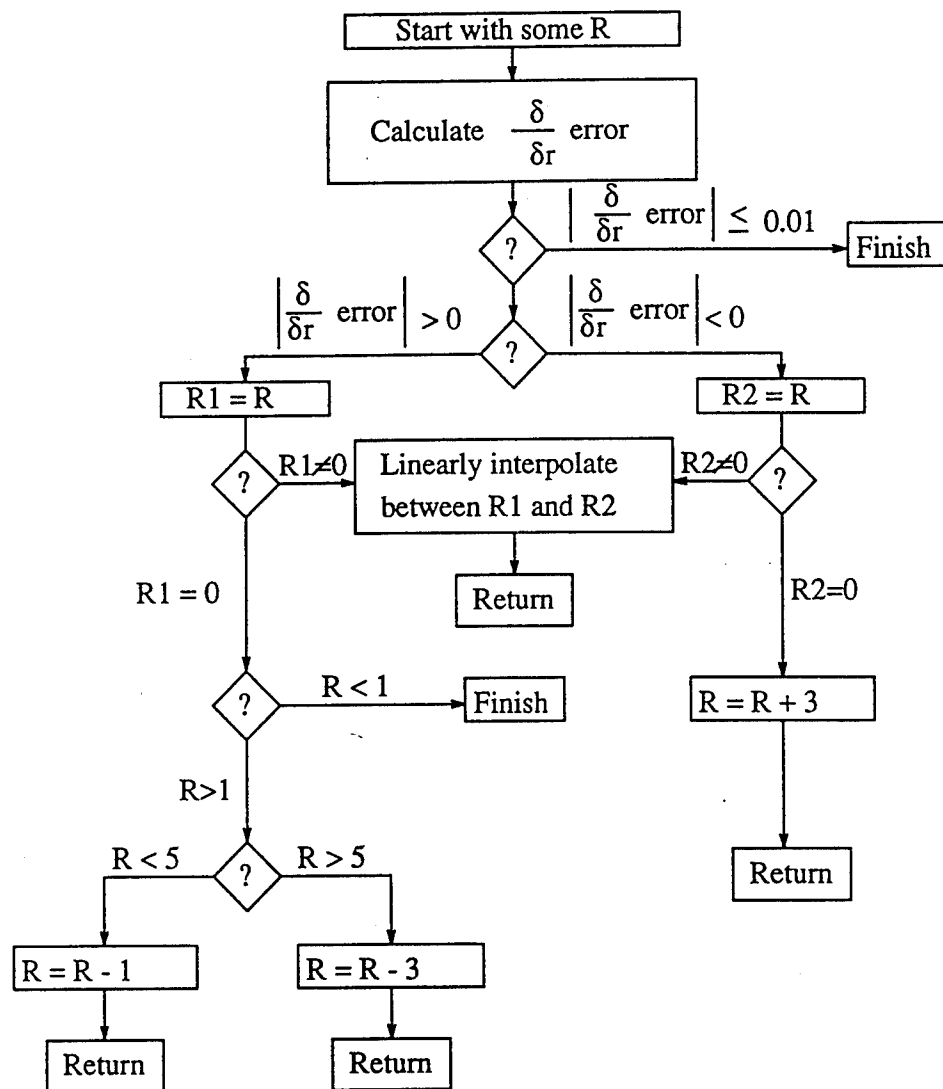


Figure A.1. Flow diagram for the windspeed algorithm used to calculate ocean surface windspeed and rain rate from SFMR data

REFERENCES

- [1] Ulaby, F.T., R.K. Moore, and A.K. Fung. *Microwave Remote Sensing*, volume 1. Artech House Inc., Norwood, MA, 1977.
- [2] Ulaby, F.T., R.K. Moore, and A.K. Fung. *Microwave Remote Sensing; Active and Passive*, volume 3. Artech House, Norwood, MA, 1982.
- [3] Fetterer, F.M. and J. D. Hawkins. An AVVHRR data set for the arctic leads ARI. Technical report, Naval Oceanographic and Atmospheric Laboratory, Stennis Space Center, Mississippi, 1991.
- [4] Orvig, S., editor. *Climates of the Polar Regions*, volume 14 of *World Survey of Climatology*. Elsevier Publishing Co., Amsterdam, New York, 1970.
- [5] Parkinson, C.L., J.C. Comiso, H.J. Zwally, D.J. Cavalieri, P. Gloersen, and W.J. Campbell. *Arctic Sea Ice, 1973-1976: Satellite Passive-Microwave Observations*. NASA Scientific and Technical Information Branch, Washington, D.C., 1987.
- [6] Swift, C.T., D.C. DeHority, and A.B. Tanner. Passive microwave spectral emission from saline ice at C-band during the growth phase. *IEEE Transactions on Geoscience and Remote Sensing*, GE-24(6):840-848, 1986.
- [7] Arcone, S.A., A.J. Gow, and S. McGrew. Microwave dielectric, structural, and salinity properties of simulated sea ice. *IEEE Transactions on Geoscience and Remote Sensing*, GE-24(6):832-839, 1986.
- [8] Grenfell, T.C. and J.C. Comiso. Multifrequency passive microwave observations in first-year sea ice grown in a tank. *IEEE Transactions on Geoscience and Remote Sensing*, GE-24(6):826-831, 1986.
- [9] St.Germain, K.M., C.T. Swift, and T.G. Grenfell. Determination of dielectric constant of young sea ice using microwave spectral radiometry. *Journal of Geophysical Research*, in press, 1992.
- [10] Cavalieri, D.J., P. Gloersen, and W.J. Campbell. Determination of sea ice parameters with the Nimbus 7 SMMR. *Journal of Geophysical Research*, 89:5355-5369, 1984.
- [11] Hollinger, J., R. Lo, G. Poe, R. Savage, and J. Pierce. Special Sensor Microwave Imager users guide. Technical report, Naval Research Laboratory, Washington D.C., 1987.

- [12] Hollinger, J.P., J.L. Pierce, and G.A. Poe. SSM/I instrument evaluation. *IEEE Transactions on Geoscience and Remote Sensing*, GE-28(5):781-790, 1990.
- [13] Goodberlet, M.A. and C.T. Swift. Remote sensing of ocean surface winds with the Special Sensor Microwave/Imager. *Journal of Geophysical Research*, 94(C10):14,547-14,555, 1989.
- [14] Swift, C.T., L.S. Fedor, and R.O. Ramseier. An algorithm to measure sea ice concentration with microwave radiometers. *Journal of Geophysical Research*, 90(C1):1087-1099, 1985.
- [15] Grenfell, T.C., D.L. Bell, A.W. Lohanick, C.T. Swift, and K.M. St.Germain. Multifrequency passive microwave observation of saline ice grown in a tank. In *Proceedings of International Geoscience and Remote Sensing Symposium*, pages 1687-1690, Edinburgh, Scotland, September 1988.
- [16] Thorndike, A.S. and R. Colony. Arctic ocean buoy data report, 1 January 1979 - 31 December 1979. Technical report, University of Washington, Polar Science Center, Seattle, Washington, 1980.
- [17] Key, J. and M. Haeffliger. Arctic ice surface temperature retrieval from AVHRR thermal channels. *Journal of Geophysical Research*, 97:5885-5893, 1992.
- [18] Weeks, W.F. Sea ice: The potential of remote sensing. *Oceanus*, 24:39-47, 1981.
- [19] Goodberlet, M.A. *Special Sensor Microwave/Imager (SSM/I) Calibration / Validations*. PhD thesis, University of Massachusetts, 1990.
- [20] Carnahali, J.B., H.A. Luther, and J.O. Wilkes. *Applied Numerical Methods*. John Wiley & Sons, Inc., New York, 1964.
- [21] Rothrock, D.A. and D.R. Thomas. Principle component analysis of satellite microwave data over sea ice. *Journal of Geophysical Research*, 93:2321-2332, 1988.
- [22] Comiso, J.C. Arctic multiyear ice classification and summer ice cover using passive microwave satellite data. *Journal of Geophysical Research*, 95:13411-13422, 1990.